Inorganic Chemistry

pubs.acs.org/IC

Article

Ammonia–Borane Dehydrogenation Catalyzed by Dual-Mode Proton-Responsive Ir-CNN^{H} Complexes

Isabel Ortega-Lepe, Andrea Rossin,* Práxedes Sánchez, Laura L. Santos, Nuria Rendón, Eleuterio Álvarez, Joaquín López-Serrano, and Andrés Suárez*

Cite This: *Inorg. Chem.* 2021, 60, 18490–18502

Read Online

ACCESS | Metrics & More | Article Recommendations | Supporting Information

ABSTRACT: Metal complexes incorporating proton-responsive ligands have been proved to be superior catalysts in reactions involving the H_2 molecule. In this contribution, a series of Ir^{III} complexes based on lutidine-derived CNN^{H} pincers containing N-heterocyclic carbene and secondary amino NHR [R = Ph (**4a**), *t*Bu (**4b**), benzyl (**4c**)] donors as flanking groups have been synthesized and tested in the dehydrogenation of ammonia–borane (NH_3BH_3, AB) in the presence of substoichiometric amounts (2.5 equiv) of *t*BuOK. These preactivated derivatives are efficient catalysts in AB dehydrogenation in THF at room temperature, albeit significantly different reaction rates were observed. Thus, by using 0.4 mol % of **4a**, 1.0 equiv of H_2 per mole of AB was released in 8.5 min (turnover frequency ($TOF_{50\%}$) = 1875 h^{-1}), while complexes **4b** and **4c** (0.8 mol %) exhibited lower catalytic activities ($TOF_{50\%}$ = 55–60 h^{-1}). **4a** is currently the best performing Ir^{III} homogeneous catalyst for AB dehydrogenation. Kinetic rate measurements show a zero-order dependence with respect to AB, and first order with the catalyst in the dehydrogenation with **4a** ($-d[AB]/dt = k[\mathbf{4a}]$). Conversely, the reaction with **4b** is second order in AB and first order in the catalyst ($-d[AB]/dt = k[\mathbf{4b}][AB]^2$). Moreover, the reactions of the derivatives **4a** and **4b** with an excess of *t*BuOK (2.5 equiv) have been analyzed through NMR spectroscopy. For the former precursor, formation of the iridate **5** was observed as a result of a double deprotonation at the amine and the NHC pincer arm. In marked contrast, in the case of **4b**, a monodeprotonated (at the pincer NHC-arm) species **6** is observed upon reaction with *t*BuOK. Complex **6** is capable of activating H_2 reversibly to yield the trihydride derivative **7**. Finally, DFT calculations of the first AB dehydrogenation step catalyzed by **5** has been performed at the DFT//MN15 level of theory in order to get information on the predominant metal–ligand cooperation mode.

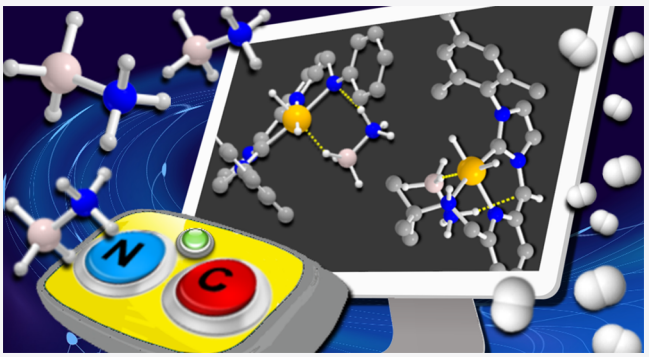

INTRODUCTION

The controlled release of H_2 from high content hydrogen compounds used as H_2-storage systems is paramount to the use of this gas as an energy vector in the so-called Hydrogen Economy.[1,2] In this context, ammonia–borane (NH_3BH_3, AB) has received increasing attention as a hydrogen storage material because of its high available hydrogen content (19.6 wt % H), moisture kinetic stability and easy H_2 thermal release.[3] In addition, AB dehydrogenation renders B–N oligomers and polymers as byproducts that are suitable starting materials for the synthesis of boron nitride (BN) ceramics.[4] Although AB dehydrogenation can be performed under simple thermal conditions,[5] insufficient kinetic control of the process leads to the formation of ill-defined B–N containing solids. This is a serious drawback for the H_2-depleted material recycling. As a consequence, catalytic approaches to the H_2 release from AB have been envisaged. The use of a catalyst allows for a fine control of the rate and extent of H_2 production, as well as the nature of the H_2-depleted byproducts. In addition, the H_2 release temperature is lowered, with respect to pure AB, and the process can be performed with a lower energetic impact.

Catalysts based on transition metals have provided fast kinetics and a large extent of H_2 release under relatively mild reaction conditions.[6] Particularly, metal complexes stabilized by pincer ligands have been widely investigated because of the enhanced catalyst stability provided by the κ^3–tridentate ligand coordination.[7−16] Moreover, since ammonia–borane is a polar molecule with hydridic (BH) and acidic (NH) hydrogen atoms, transition-metal complexes based on ligands containing Brønsted basic sites have been shown to be

Received: September 30, 2021
Published: November 16, 2021

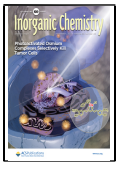

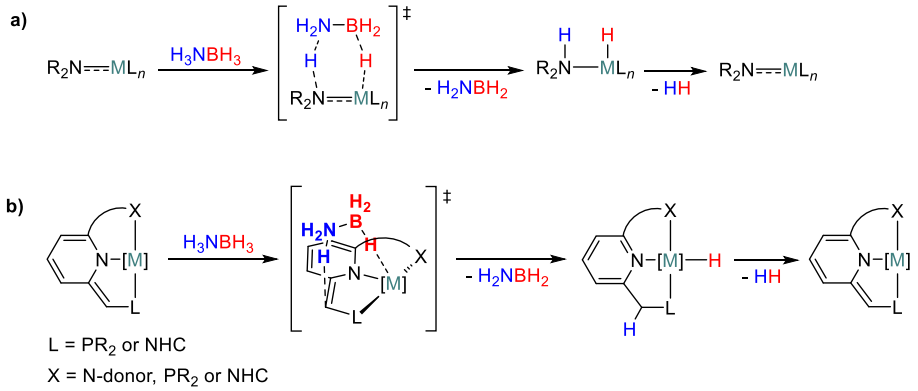

Figure 1. Proposed mechanisms for the first step of ammonia–borane dehydrogenation with transition-metal complexes based on ligands containing Brønsted basic sites.

Scheme 1. Synthesis of the Ir-CNN^H Complexes 2a, 2b, 3, and 4a–4c

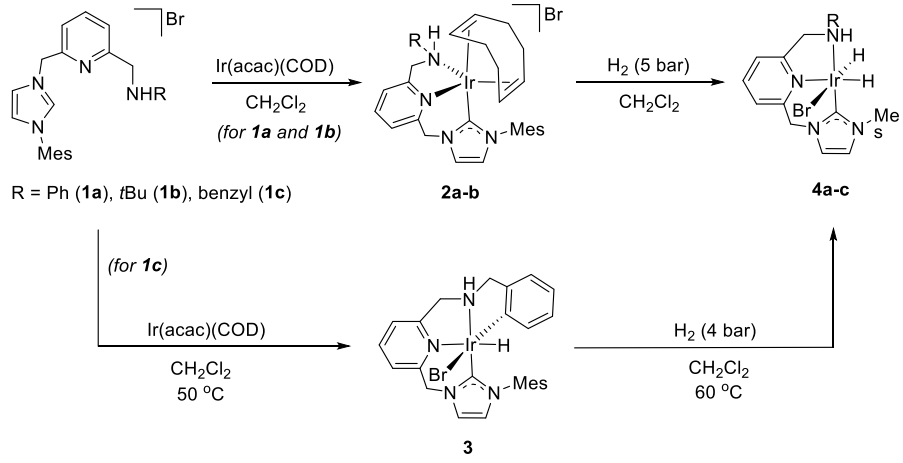

particularly adequate to promote H_2 release from AB through the transfer of the hydridic BH to the acidic metal center and the NH proton to the basic ligand functionality (bifunctional catalysts).[13−19] Prevalent examples of such systems are metal complexes based on ligands bearing secondary amine donors,[20] which are capable of getting involved in reversible metal-amine/metal-amido interconversion (Figure 1a).[13−15,17,18]

Similarly, metal complexes incorporating picoline- or lutidine-derived pincer ligands are able to participate in ligand-assisted H−X (X = H, C, O, N, B) bond activation upon deprotonation of the (acidic) CH_2 pincer side-arms and concomitant dearomatization of the N-containing ring (Figure 1b).[21] Although these derivatives have been found to be efficient catalysts in a plethora of hydrogenation reactions of polar organic substrates and alcohol dehydrogenation reactions, their application in AB dehydrogenation has been limitedly explored.[16] Moreover, development of homogeneous catalytic systems based on lutidine-derived ligands has been mainly focused on phosphine-containing PNX (X = phosphine or N-donor) pincers, albeit substitution of the flanking PR_2 groups by another strong σ-donor such as N-heterocyclic carbenes (NHCs) has also been briefly addressed. Upon deprotonation of the methylene CH_2−NHC arms, these organometallics are catalytically active in ligand-assisted processes.[22−25]

A step forward in catalysts design that has provided superior catalytic systems in hydrogenation and dehydrogenation reactions relies on the use of ligands containing two Brønsted acidic/basic sites, such as a lutidine fragment and a secondary amino group.[25,26] Since two Brønsted functionalities are present in these ligands, the related complexes might participate in ligand-assisted processes through pyridine aromatization/dearomatization or amine-metal/amido-metal interconversion. Herein, we report on the synthesis of a series of Ir complexes based on lutidine-derived CNN^H ligands bearing secondary amino and NHC side-arms and their catalytic performance in AB dehydrogenation. Detailed kinetic and NMR spectroscopy studies show that different species are formed under catalytic conditions, depending on the substituent of the secondary amino group. Moreover, DFT calculations have determined the preferred metal−ligand cooperation mode when a doubly deprotonated catalytic species is formed.

RESULTS AND DISCUSSION

Synthesis and Structure of Ir-CNN^H Complexes. Following previously reported procedures for the synthesis of Ir complexes based on related NHC-containing lutidine-derived ligands,[23,24] the diolefin derivatives **2a** and **2b** were prepared by the reactions of Ir(acac)(COD) and the N-heterocyclic carbene ligand precursors **1a** and **1b**,[25] respectively (Scheme 1). These complexes were isolated as yellow solids in good yields (99% and 77%, respectively), and spectroscopical and analytically characterized. In the ^{1}H NMR spectrum of **2a**, the olefinic hydrogens of one of the C=C moieties of the COD ligand appear as multiplets at δ 4.51 and

https://doi.org/10.1021/acs.inorgchem.1c03056
Inorg. Chem. 2021, 60, 18490−18502

4.41 ppm, whereas the resonances corresponding to the other olefin fragment are shown at δ 2.95 and 2.82 ppm. Moreover, the ^{1}H−^{1}H EXSY experiment of **2a** recorded at 298 K exhibits intense cross-peaks corresponding to the pairwise exchange of the olefinic signals corresponding to different C═C moieties. The observed dynamic behavior can be assigned to alkene site exchange involving the decoordination of one of the olefin fragments to produce a distorted tetrahedral intermediate, and subsequent recoordination of the uncoordinated C═C group to the opposite side (see the Supporting Information).[23] Meanwhile, the C-2 of the NHC ligand fragment produces a singlet at δ_C 181.0 ppm in the ^{13}C{^{1}H} NMR spectrum. Similar NMR data and fluxional behavior were shown by complex **2b**.

Conversely, heating a CH_2Cl_2 solution of Ir(acac)(COD) and the imidazolium salt **1c** to 50 °C produced the expected coordination of the lutidine-derived CNN^H pincer ligand along with the activation of one *ortho* C−H bond of the benzyl substituent, yielding the κ^4-(C^{NHC},N^{Py},N^{amine},C^{aryl}) complex **3** (Scheme 1). The solid-state structure of this derivative was determined by single-crystal X-ray diffraction (Figure 2). The complex is comprised of a stereogenic Ir center in an octahedral coordination geometry, in which the carbene carbon and the nitrogen donors of the CNN^H ligand are coordinated in the meridional positions, as defined by the C_{NHC}−Ir-N_{amine} angle of 171.0°, and the metalated aryl fragment is located *trans* to the Br atom (C_{aryl}−Ir-Br = 169.1°).

Complexes **2a** and **2b** reacted with H_2 (5 bar) in CH_2Cl_2, resulting in the formation of the bromodihydride complexes **4a** and **4b**, respectively (Scheme 1). Similarly, derivative **4c** was obtained by exposing a CH_2Cl_2 solution of **3** at 60 °C to 4 bar of H_2. Complexes **4a**−**4c**, which were isolated as air-stable yellow solids, were characterized analytically and spectroscopically. For example, in the ^{1}H NMR spectrum of complex **4a**, two mutually coupled doublets are detected in the hydride region, appearing at −19.05 and −23.25 ppm ($^2J_{HH}$ = 6.9 Hz), which are assigned to the IrH hydrogens located *trans* and *cis* to the pyridine fragment, respectively, as determined by ^{1}H−^{1}H NOESY spectroscopy. In the same experiment, the NH hydrogen produces a broad doublet resonance at 6.15 ppm ($^3J_{HH}$ = 11.1 Hz). In the ^{13}C{^{1}H} NMR spectrum, diagnostic signals for complex **4a** are shown at 153.5 ppm, caused by the carbene carbon, and at 62.2 and 55.3 ppm, corresponding to the methylene NH- and NHC-arms of the pincer, respectively. Analogous NMR data were observed in the case of complexes **4b** and **4c**, with the notable exception of the resonances due to the NH groups in the ^{1}H NMR spectra, which are shifted upfield, with respect to that of **4a**, appearing as a broad doublet of doublets at 4.03 ppm ($^3J_{HH}$ = 12.5 Hz, $^3J_{HH}$ = 3.2 Hz) for **4b**, and 4.39 ppm ($^3J_{HH}$ = 9.2 Hz, $^3J_{HH}$ = 9.2 Hz) in the case of **4c**.

The solid-state structure of **4b**, as determined by single-crystal X-ray diffraction, exhibits an octahedral geometry with the CNN^H pincer adopting a meridional coordination and the two hydride ligands in *cis* to each other (Figure 3). Moreover,

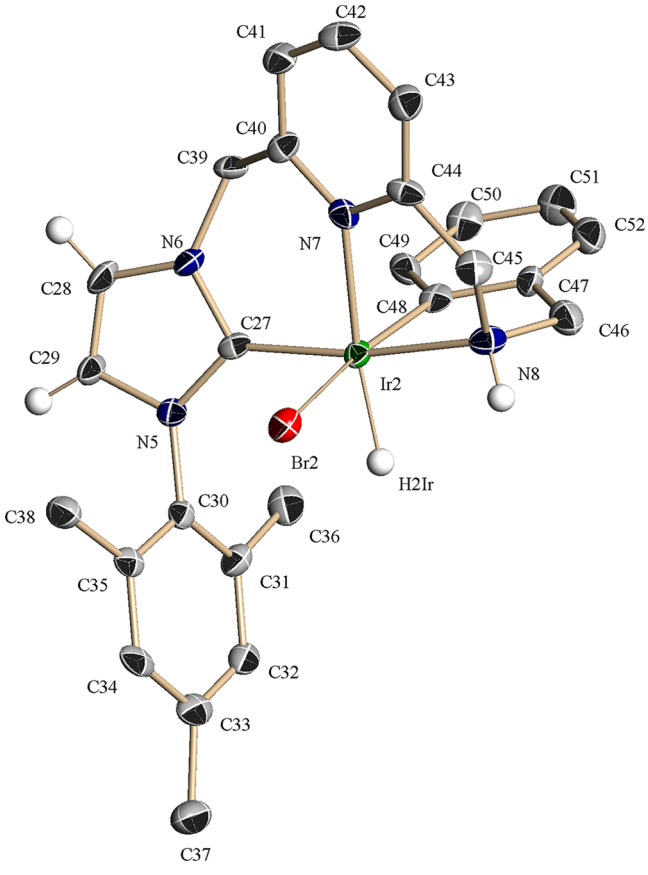

Figure 2. ORTEP drawing at 30% ellipsoid probability of complex **3**. Hydrogen atoms (except for the hydride ligand and the NHC and NH hydrogens) have been omitted for clarity. Selected bond lengths: Ir(2)−C(27), 1.959(10) Å; Ir(2)−N(7), 2.124(7) Å; Ir(2)−N(8), 2.132(8) Å; Ir(2)−Br(2), 2.6266(11) Å; and Ir(2)−C(48), 2.010(10) Å. Selected bond angles: C(27)−Ir(2)−N(8), 171.0(3)°; C(27)−Ir(2)−C(48), 97.4(4)°; C(27)−Ir(2)−N(7), 91.4(3)°; N(8)−Ir(2)−N(7), 79.7(3)°; and C(48)−Ir(2)−Br(2), 169.1(3)°.

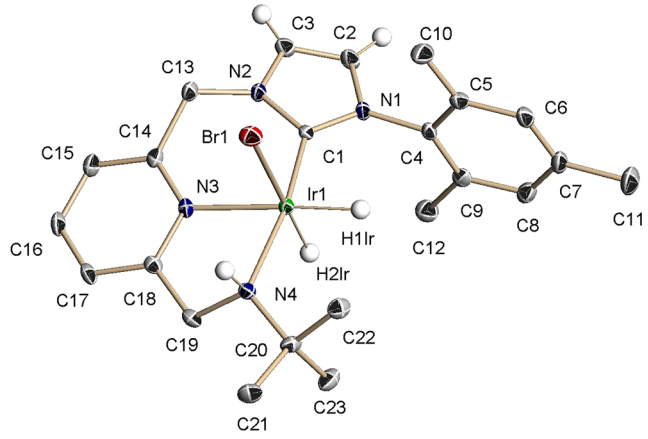

Figure 3. ORTEP drawing at 30% ellipsoid probability of complex **4b**. Hydrogen atoms (except for the hydride ligands and the NHC and NH hydrogens) have been omitted for clarity. Selected bond lengths: Ir(1)−C(1), 1.939(3) Å; Ir(1)−N(3), 2.116(3) Å; Ir(1)−N(4), 2.184(3) Å; Ir(1)−Br(1), 2.6385(4) Å; Ir(1)-H(1Ir), 1.569(18) Å; and Ir(1)−H(2Ir), 1.591(18) Å. Selected bond angles: C(1)−Ir(1)−N(4), 169.62(12)°; C(1)−Ir(1)−N(3), 91.83(12)°; N(3)−Ir(1)−Br(1), 88.86(8)°; and N(4)−Ir(1)−N(3), 78.04(10).

the existence of a hydrogen bond between the bromine ligand and the amino hydrogen is evident from the H···Br distance of 2.76 Å, which is shorter than the sum of the van der Waals radii of H and Br (2.97 Å).[27]

AB Dehydrogenation. Complexes **4a**−**4c** were tested as catalysts in the dehydrogenation of ammonia borane after a preliminary activation with *t*BuOK (see the Supporting

https://doi.org/10.1021/acs.inorgchem.1c03056
Inorg. Chem. 2021, 60, 18490−18502

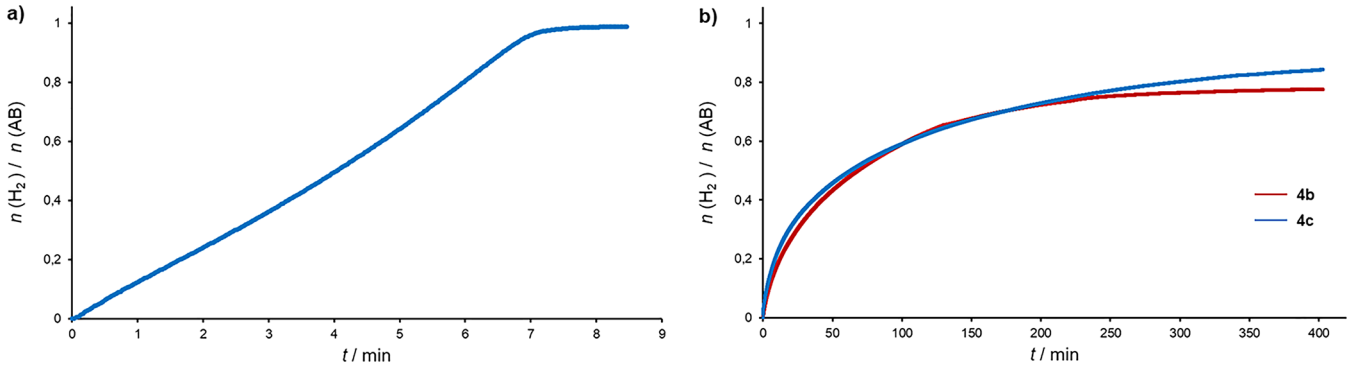

Figure 4. H_2 evolution in the catalytic dehydrogenation of AB with (a) **4a** (0.4 mol %) and (b) **4b** and **4c** (0.8 mol %). Conditions: THF, room temperature, *t*BuOK:**4** = 2.5, [AB] = 1.6 M.

Information for the experimental setup). The initial treatment with a base is necessary to trigger the catalysis; bare complex **4a** (without a base) was tested in AB dehydrogenation, and it was found to be a poor catalyst (initial turnover frequency (TOF) of <5 h^{-1}). Upon addition of a THF solution of **4a** (0.4 mol %) and *t*BuOK (base:**4a** = 2.5) to a stirred AB solution in the same solvent, instantaneous vigorous gas evolution was observed, followed by the immediate formation of an off-white precipitate. Follow-up of the reaction by measuring the pressure increase in the system showed that 1.0 equiv of H_2 per AB molecule was released in ca. 8.5 min at room temperature (Figure 4a). To the best of our knowledge, the high room-temperature catalytic activity of **4a** (TOF = 1764 h^{-1}) is only surpassed by the cationic Pd complexes [Pd(allyl)][BF_4], [Pd(allyl)(2,4-hexadiene)][BF_4] and [Pd-$(MeCN)_4$][BF_4]$_2$ reported by the group of Michalak in 2010,[28] and by the Ru-PN^HP and $RuCl_2(PN)_2$ derivatives reported by the Schneider group in 2009[13] and the Fagnou group in 2008,[17] respectively. Note that the catalytic activity of **4a** is slightly superior to that of the most active Ir-based catalyst reported to date: IrH_2(POCOP), published by Goldberg and colleagues in 2006.[7] Thus, **4a** is currently the best-performing iridium-containing homogeneous catalyst for AB dehydrogenation. On the other hand, reactions performed with complexes **4b** and **4c**, using 0.8 mol % of catalyst loading under the same reaction conditions, yielded ca. 0.75−0.8 equiv of H_2 in 5 h (for **4b**, $TOF_{50\%}$ = 55 h^{-1}; for **4c**, $TOF_{50\%}$ = 60 h^{-1}); thus, both catalysts exhibit significantly lower catalytic activity than **4a** (Figure 4b).

The registered ATR-IR spectrum of the insoluble H_2-depleted material produced in the AB dehydrogenation reactions with **4a** (amounting to >95% of the total BN byproducts, as estimated by mass balance) contains peaks corresponding to the N−H (3299 and 3248 cm^{-1}) and B−H (2384 and 2313 cm^{-1}) stretching modes (see Figure S7 in the Supporting Information). These absorptions, as well as the spectrum fingerprint, closely resemble those described for the mainly linear poly(aminoboranes), $[NH_2BH_2]_n$, isolated from the dehydrogenation of AB with Brookhart's Ir-POCOP complex,[29] and Ru- and Fe-PN^HP complexes.[13,14] The ^{11}B NMR spectrum of the soluble part of the reaction with **4a** exhibits broad signals between δ_B 17−31 ppm, in agreement with the formation of species resulting from the release of more than 1 equiv of H_2 (see Figure S8 in the Supporting Information). However, the small fraction of these products is not enough to account for an overall H_2 yield exceeding 1.0 equiv.

The observed differences in the catalytic activity provided by **4a** and complexes **4b** and **4c** led us to determine the reaction kinetic laws. For **4a**, plotting of $[AB]_o-[AB]$ versus time gave a straight line (k_{obs} = 3.4 × 10^{-3} M s^{-1}), indicative of a pseudo-zero order relationship in AB (see Figures S10 and S11 in the Supporting Information). Initial rate experiments performed at different catalyst concentrations showed that hydrogen release has a first-order rate dependence in **4a** (Figure S12 in the Supporting Information). The observed lack of dependence on AB concentration is in agreement with its rapid reaction with the catalyst and, therefore, with a rate-determining step that does not involve AB activation.

Next, kinetic isotope effects (KIE) values were determined using the deuterated AB isotopologues (NH_3BD_3, ND_3BH_3, and ND_3BD_3). A pronounced decrease in the reaction rate was observed with the N-deuterated substrate [ND_3BH_3, k_H/k_D = 8.4], while deuteration at boron produces a somewhat lower rate [NH_3BD_3, k_H/k_D = 1.4]. In the case of full AB deuteration, within the experimental error, the KIE is the product of the individual isotope effects measured with ND_3BH_3 and NH_3BD_3 [ND_3BD_3, k_H/k_D = 13.4]. This suggests a concerted, asynchronous transition state in the cleavage of the N−H and B−H bonds. However, this conclusion is tentative, since the observed KIEs should reflect the contributions of all the multiple steps of the catalytic cycle. We must bear in mind that AB activation does *not* seem to be the rate-determining step.[30]

The kinetic law was also inferred for the reaction with the catalyst precursor **4b**. From the initial rate experiments performed at different AB and catalyst concentrations, a kinetic lawd[AB]/d*t* = $k_{obs}[AB]^2$ = k[**4b**][AB]^2 (k_{obs} = 1.3 × 10^{-4} M^{-1} s^{-1}) was revealed, evidencing different rate laws for the reactions with complexes **4a** and **4b** (see Figures S14 and S15 in the Supporting Information). For the latter catalyst, the KIE values using deuterated NH_3BD_3, ND_3BH_3, and ND_3BD_3 were found to be 2.5, 2.8, and 7.7, respectively. These data suggest a mechanism where two AB molecules are involved in the rate-limiting step,[12] with the N−H and B−H bonds splitting occurring in a concerted manner.

Mechanistic Insights. Taking into account previous studies with catalysts based on proton-responsive ligands,[13,14,16,17] a plausible mechanism for AB dehydrogenation catalyzed by complexes **4** in the presence of an auxiliary base should involve initial hydrogen transfer from AB to the deprotonated form of the Ir-CNN^H catalyst precursors with the concomitant formation of the "inorganic ethylene analogue" $BH_2{=}NH_2$, followed by ligand-assisted H_2 elimination. Therefore, to gain insight into the species formed upon

https://doi.org/10.1021/acs.inorgchem.1c03056
Inorg. Chem. 2021, 60, 18490−18502

treatment of complexes **4** with a base, derivative **4a** was initially reacted with *t*BuOK (2.5 equiv) in THF-d_8 (Scheme 2).

Scheme 2. Formation of Iridate Complex 5

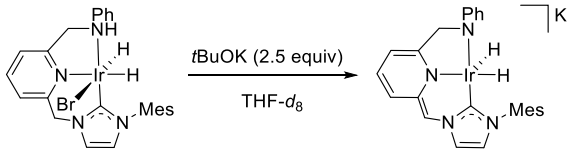

4a **5**

Reaction of the Ir-CNN^H derivatives with a strong base could induce deprotonation of the pincer ligand at its methylene carbon in the side arm[22−25] and/or at the secondary amino group.[20,25,31] Analysis of the deuterated solution through NMR spectroscopy showed the formation of a major species (ca. 90%), which was characterized as the highly air-sensitive amido iridate(III) **5**,[32] confirming the deprotonation of both the NH and the NHC−methylene arm of **4a**. The ^{1}H NMR spectrum of **5** features two mutually coupled doublets at δ −16.35 ppm and δ −18.61 ppm ($^2J_{HH}$ = 5.5 Hz), corresponding to the hydride ligands. In the same experiment, the methylene CH_2NPh hydrogens appear as doublets at δ 4.24 and 3.80 ppm ($^2J_{HH}$ = 16.5 Hz), while the methine CH-NHC hydrogen is a singlet at δ 6.25 ppm. In the ^{13}C{^{1}H} NMR spectrum, the carbene carbon produces a singlet at δ_C 156.8 ppm, whereas the CH_2N and CH-NHC bridges of the pincer give rise to resonances at δ_C 64.2 and 49.0 ppm, respectively.

Crystals suitable for X-ray diffraction (XRD) analysis of **5** were obtained by cooling the above THF-d_8 solution to −30 °C (Figure 5). The X-ray data confirmed the initially proposed structure. The potassium iridate **5** is dimeric in the solid state, and the two Ir centers are bound to the opposite ligands through the deprotonated CH-NHC arms. The Ir atoms are in an octahedral coordination geometry, with the pincer and one hydride ligand occupying the meridional plane [Σ(Ir) = 361.2°] and the other IrH hydrogen and the Ir(CNN*)H_2 unit coordinated at the apical positions. The K^+ counterions are surrounded by two molecules of THF ($d_{(K-O)}$ = 2.61 Å, avg.), an η^4-coordinated mesityl ring (K−C distances of 3.30−3.39 Å), one carbon of the *N*-phenyl ring ($d_{(K-C)}$ = 3.14 Å), and the meridional hydride ligand ($d_{(K-H)}$ = 2.85 Å). The observed dinuclear solid-state structure of **5** should be favored by the large planarity of the deprotonated Ir-CNN* fragments.

Although in the solid state, complex **5** can be regarded as a dimer, the structure of **5** in solution is that of a monomer, as evidenced by diffusion NMR studies.[33] The ^{1}H DOSY experiment of **5** afforded a diffusion coefficient D = 7.2 × 10^{-10} m^2/s (log D = −9.14) from which a value of its hydrodynamic radius (r_H) of 6.4 Å was estimated using the Stokes−Einstein equation. The radius for the dimeric structure calculated from its X-ray volume[34] was $r_{X\text{-}ray}$ = 13.9 Å, which is approximately twice the r_H of **5** in solution. Moreover, the diffusion coefficient D of **5** is very similar to that obtained for **4a** using ^{1}H DOSY spectroscopy [D = 8.2 × 10^{-10} m^2/s; log D = −9.09; r_H = 5.5 Å]. This further supports the existence of a monomeric form of **5** in solution.

In marked contrast, under the conditions used for the formation of **5**, reaction of **4b** with *t*BuOK (2.5 equiv) in THF-d_8 gave rise to complex **6** (75%−80% NMR yield), which is selectively deprotonated at the NHC-bridge, as determined through NMR spectroscopy (Scheme 3). The ^{1}H NMR

Scheme 3. Formation of Deprotonated Complex 6 and Trihydride Derivative 7

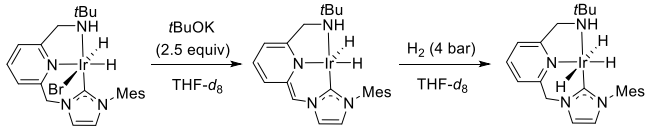

4b **6** **7**

experiment of **6** shows, in the hydride region, two mutually coupled doublets appearing at −16.49 and −18.41 ppm ($^2J_{HH}$ = 5.6 Hz). Moreover, in the same spectrum, a doublet of

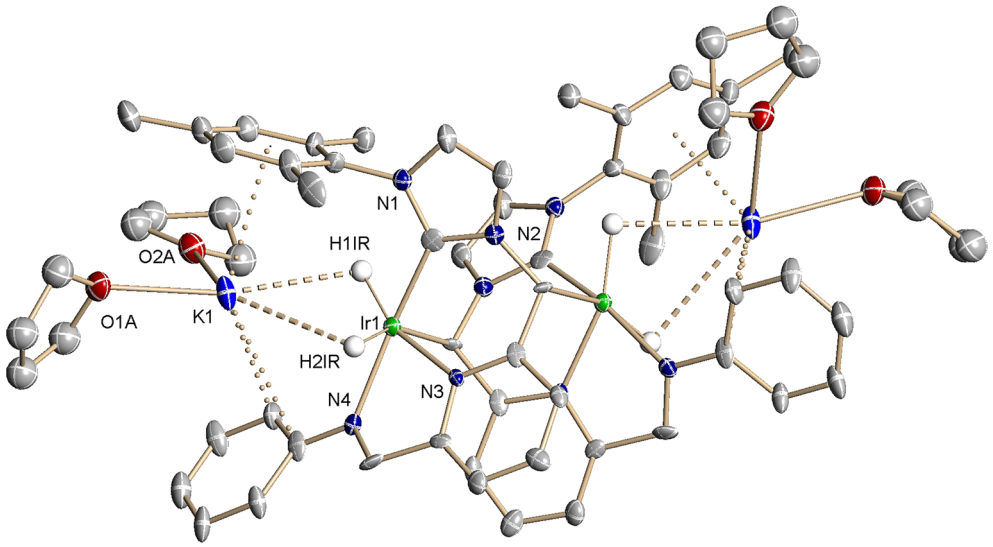

Figure 5. ORTEP drawing at 30% ellipsoid probability of the dimeric form of complex **5**. Hydrogen atoms (except for the hydride ligands) have been omitted for clarity. Selected bond lengths: Ir(1)−C(1), 1.999(19) Å; Ir(1)−N(3), 2.033(13) Å; Ir(1)−N(4), 2.115(15) Å; and Ir(1)−C(13), 2.215(17) Å. Selected bond angles: C(1)−Ir(1)−N(4), 165.9(7)°; C(1)−Ir(1)−N(3), 90.4(7)°; N(3)−Ir(1)−N(4), 78.5(6)°; C(1)−Ir(1)−C(13), 98.9(6)°; and N(4)−Ir(1)−C(13), 90.6(6)°.

https://doi.org/10.1021/acs.inorgchem.1c03056
Inorg. Chem. 2021, 60, 18490−18502

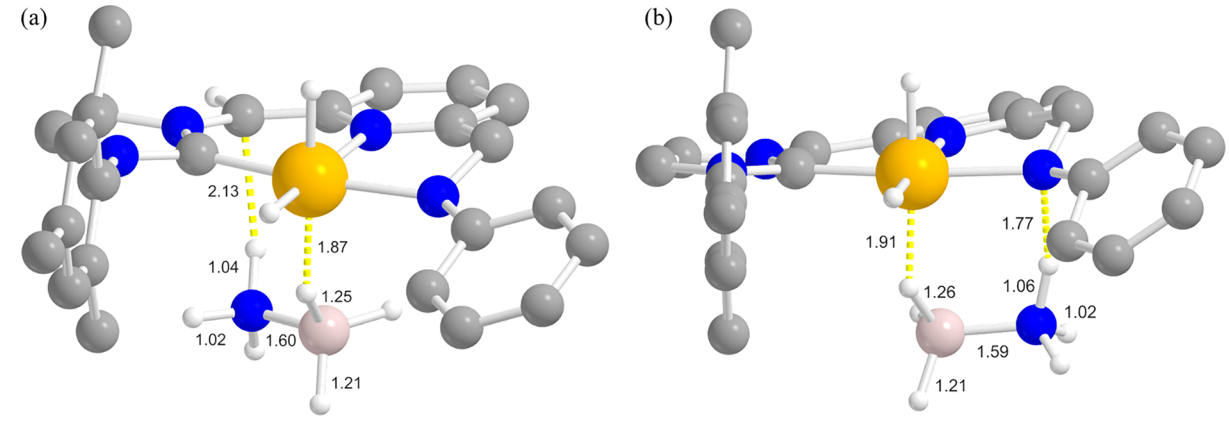

Figure 6. Optimized structure of (CNN*)$IrH_2(\eta^1$-*BH*-AB) with (a) NH_3 interaction with the carbanionic C atom (**Ia**) and (b) with NH_3 interaction with the amido N atom (**Ib**). Selected optimized bond lengths are reported in Ångstroms. H atoms on the pincer ligand not relevant for the discussion are omitted for clarity. Atom color code: white, H; gray, C; blue, N; pink, B; orange, Ir.

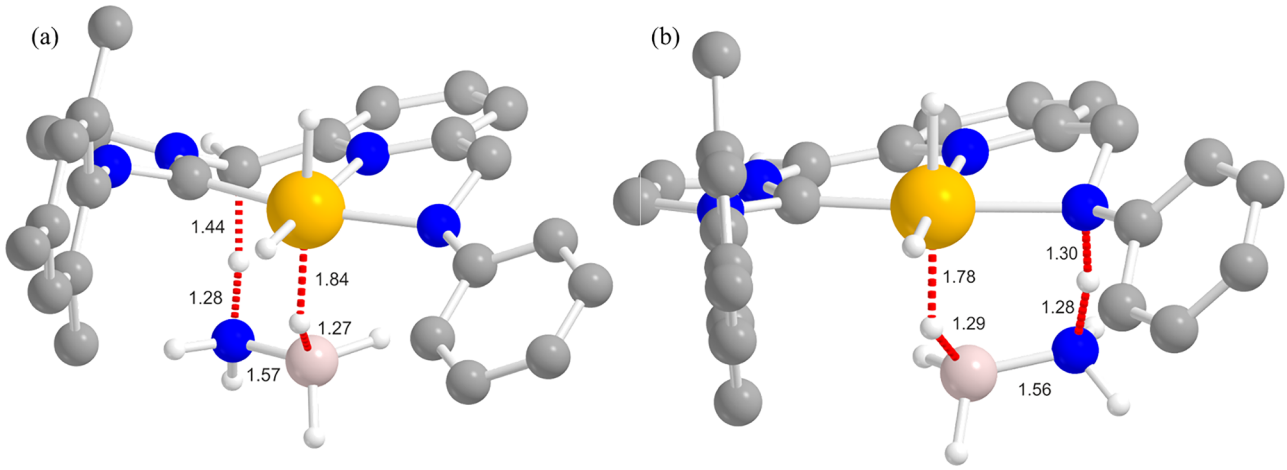

Figure 7. Optimized structures of (a) $\mathbf{TS_{1C}}$ (from **Ia**) and (b) $\mathbf{TS_{1N}}$ (from **Ib**). Selected optimized bond lengths are reported in Ångstroms. H atoms on the pincer ligand not relevant for the discussion are omitted for clarity. Bonds involved in the TS transformation depicted as red dotted lines. See Figure 6 for the atom color code.

doublets at 3.88 ppm ($^2J_{HH}$ = 13.6 Hz, $^3J_{HH}$ = 2.8 Hz) and a multiplet at 3.39 ppm, corresponding to the CH_2N hydrogens, and a broad doublet at δ 2.97 ppm ($^2J_{HH}$ = 10.9 Hz) due to the NH, are also observed; whereas, the proton of the deprotonated methine-NHC arm produces a singlet at 5.48 ppm. In the $^{13}C\{^1H\}$ NMR spectrum of **6**, the carbene carbon appears as a singlet at 150.0 ppm, while the N- and NHC-linkers of the pincer produce singlet resonances at 56.1 and 54.9 ppm, respectively. Further attempts to perform the deprotonation of the amino group of **4b** were unsuccessful, likely due to the reduced NH acidity, in comparison to **4a**.

Because of the fast kinetics, attempts to detect metallic intermediates through NMR spectroscopy during the dehydrogenation reaction catalyzed by **4a** at room temperature were unsuccessful. However, at the end of the catalytic process, the main metal-containing species present in solution (>90%, from ^1H NMR analysis) is the amido iridate(III) **5**. Moreover, pressurization of a THF-d_8 solution of **5** with H_2 (4 bar) did not lead to the formation of new observable species (i.e., a trihydride Ir complex).

For **4b**, the solution composition at the end of the dehydrogenation process, performed at the NMR scale in THF-d_8, is more complex than that found for **4a**: the ^1H NMR spectrum of the reaction mixture reveals the presence of NHC-deprotonated iridium dihydride **6** as the major component (ca. 30%), together with at least four other unidentified Ir hydrides. In addition, reaction in THF-d_8 of the in situ formed complex **6** with H_2 (4 bar, 48 h) produced the selective formation of trihydride derivative **7**, which is only stable under a hydrogen atmosphere (Scheme 3). Complex **7** gives rise in the hydride region of the ^1H NMR spectrum to a multiplet signal integrating for 2H at −8.92 ppm, corresponding to the apical IrH hydrogens, and a doublet of doublets at −18.24 ppm ($^2J_{HH}$ = 5.2, 5.2 Hz) that integrates for 1H, ascribed to the meridional hydride ligand. Moreover, the reprotonation of the pincer ligand side arm was confirmed from the presence of two mutually coupled doublets appearing at 5.02 and 5.10 ppm ($^2J_{HH}$ = 13.5 Hz), corresponding to the methylene−NHC pincer arm.

DFT Calculations of the First AB Dehydrogenation Step. To get further insight into the reaction catalyzed by **4a**, DFT calculations on the first step of the AB dehydrogenation mechanism were performed at the DFT//MN15 level of theory on the real structure of the supposed active catalytic species **5**, dimeric in the solid state (as found in the crystal structure determined from X-ray data collection) but monomeric in THF solution (as confirmed by DOSY NMR experiments). In this structure, possibly in the form of a THF

https://doi.org/10.1021/acs.inorgchem.1c03056
Inorg. Chem. 2021, 60, 18490−18502

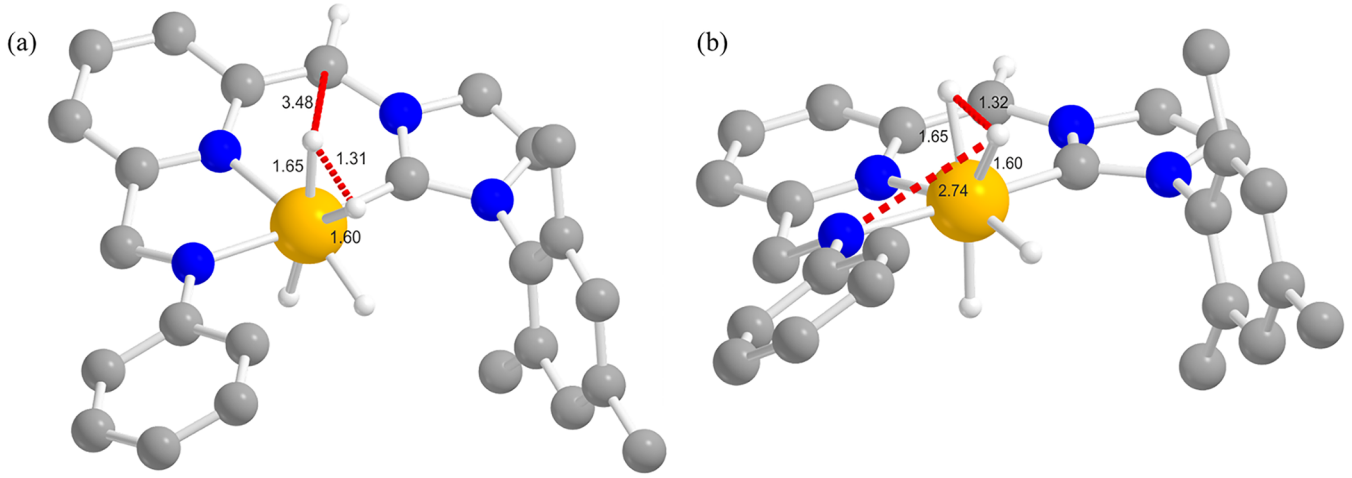

Figure 8. Optimized structures of (a) $\mathbf{TS_{2C}}$ (from **IIa**) and (b) $\mathbf{TS_{2N}}$ (from **IIb**). Selected optimized bond lengths are reported in Ångstroms. H atoms on the pincer ligand not relevant for the discussion are omitted for clarity. Bonds involved in the TS transformation depicted in red dotted lines. See Figure 6 for the atom color code.

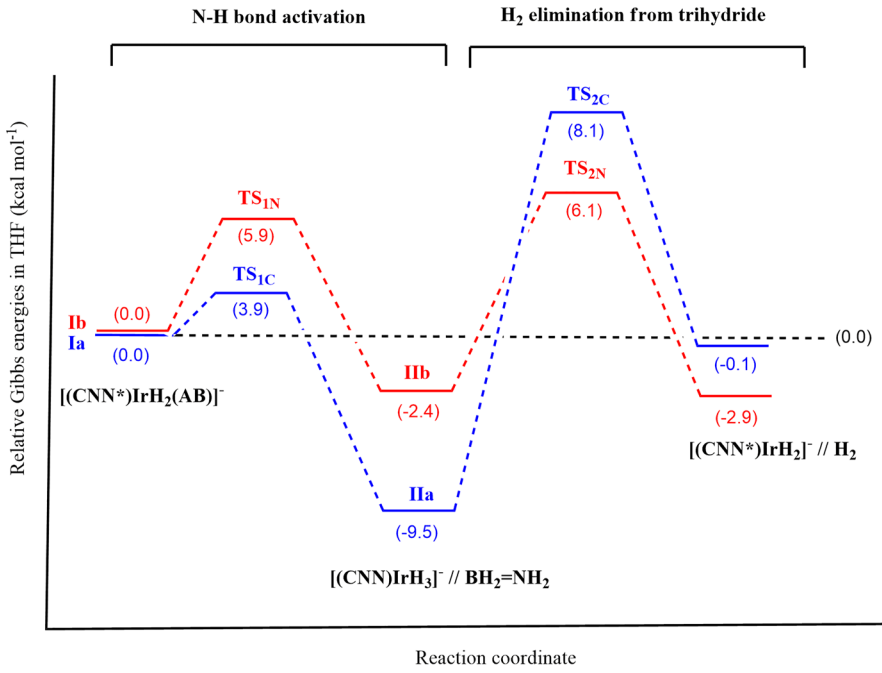

Figure 9. Gibbs energy (THF) vs. reaction coordinate profiles for the first AB dehydrogenation step mediated by **Ia** (blue line) and **Ib** (red line).

adduct with general formula $[(CNN^*)IrH_2(thf)]^-$, the solvent O atom occupies the empty coordination site *trans* to one of the hydride ligands, with the Ir^{III} ion in an octahedral coordination geometry. Successive THF/AB exchange in the metal coordination sphere is thermodynamically favored, leading to the complex $[(CNN^*)IrH_2(AB)]^-$ (**I**, Figure 6). For this complex, two different isomeric forms are conceivable, depending on the interaction site of AB NH_3 end. While the BH_3 end is always directly bound to the metal center in a η^1-fashion, the NH_3 end may be interacting either with the carbanionic C atom on the pincer skeleton ("C-path") or with the negative N atom of the NPh^- amido side arm ("N-path"). In principle, both sites are nucleophilic and both interactions are possible. No interaction with the central pyridine N atom or with the carbene arm was found. This is the typical example of "bifunctional catalyst" bearing an acidic (Ir^{III}) and a basic (CH^-/NPh^-) reactive site at the same time, where the metal center and the pincer ligand act cooperatively to extract hydrogen from AB. This class of compound is widespread in the literature, and it has been frequently exploited in the dehydrogenation of BN lightweight inorganic hydrides.[13,14,16−19] The analysis of the relative stability of the two isomers **Ia** (HC···H−N interaction, Figure 6a) and **Ib** (PhN···H−N interaction, Figure 6b) revealed that the latter is slightly more stable [ΔG_{THF}(**Ia**/**Ib**) = −2.9 kcal/mol]. Given the small Gibbs energy difference between the two isomers, both forms were taken into account for the calculation of the reaction profiles. Consistent with the kinetic data from the KIE experiments, a simultaneous BH/NH bond activation occurs and the B−H bond activation is less difficult than that of the N−H bond, since AB coordination to the metal ion through its BH_3 end is responsible for a B−H bond "preliminary" weakening. Indeed, in **I**, the B−H bond is already partially

https://doi.org/10.1021/acs.inorgchem.1c03056
Inorg. Chem. 2021, 60, 18490−18502

broken, as witnessed by the longer B−H distance on the coordinated bond if compared with the other two.

From this initial geometry, a transition state $\mathbf{TS_{1C}}/\mathbf{TS_{1N}}$ of the CH^-/NPh^- protonation by NH_3 could be found at $\Delta G^{\#}_{THF}$ = 3.9/5.9 kcal/mol along the d(N−H···CH)/d(N−H···NPh) reaction coordinate (Figure 7), with related "inorganic ethylene analogue" ($BH_2{=}NH_2$) evolution and formation of the trihydride complex $[(CNN)IrH_3]^-$ (**II**). Thermodynamics for this step is favorable in both cases, with ΔG_{THF} = −9.5 and −2.4 kcal/mol for CH^- and NPh^- protonation, respectively.

From **II** (again, in two isomeric forms **IIa** and **IIb**, depending on the protonated group of choice), different reaction paths were then considered. No H_2 formation (nonclassical hydride) from the (classical) hydride ligands with concomitant $Ir^{III} \rightarrow Ir^{I}$ reduction could be observed, at the computational level used in this study. The same can be said for a direct interaction of the hydride ligands of **II** with $BH_2{=}NH_2$; all the plausible geometries built *in silico* led to repulsive interactions and no maxima could be located on the corresponding reaction energy scan. The only mechanism featured by the presence of a maximum along the examined reaction coordinate is the direct H_2 elimination from one hydride ligand on iridium and from the methylenic $-CH_2-$ side arm (**IIa**) or from the NHPh group (**IIb**), to regenerate the starting active species **5** and close the catalytic cycle. The corresponding transition states $\mathbf{TS_{2C}}$ and $\mathbf{TS_{2N}}$ are located at 17.6 and 8.5 kcal/mol above **IIa** and **IIb**, respectively (Figure 8). The overall *G* versus reaction coordinate profiles at comparison are reported in Figure 9. From the inspection of the two profiles, we can conclude that for this complex the "N path" (red trace) is to be preferred to the "C path" (blue trace), from both a kinetic ($\Delta G^{\#}$) and a thermodynamic (ΔG) viewpoint. In addition, the rate-determining step in both cases is H_2 elimination from the trihydride intermediate **II** rather than the easy AB activation by the bifunctional complex **I**. This result is consistent with the zero-order dependence of the reaction rate from AB concentration found experimentally, since AB is not involved in the rate-determining step.

As for **4b**, the adduct of the activated neutral species **6** with two AB molecules is thermodynamically favored: ΔG_{THF} for the mono- and bis(AB) adducts equal −1.4 and −0.7 kcal/mol, respectively. The result is in agreement with the experimental evidence of a second-order kinetic dependence from AB concentration. This interaction leads to the geometry **III** (Figure S49), where the first AB molecule sits in the empty coordination site of the five-coordinated **6** interacting through its BH and NH ends with iridium and the deprotonated side arm, respectively [optimized d(Ir···H−B) = 1.88 Å; optimized d(H−C···H−N) = 2.21 Å]. The second AB molecule weakly interacts with the two hydrides on the metal center to the opposite side of the Ir(CNN) plane [optimized $d(Ir-H_{axial}\cdots H-B)$ = 2.86 Å; optimized $d(Ir-H_{equatorial}\cdots H-N)$ = 1.74 Å]. No interaction between AB and the NH*t*Bu group is observed. Therefore, this part of the complex is not involved in the catalytic process and no "N path" can be conceived, at odds with its phenyl-substituted analogue. Unfortunately, no plausible reaction mechanism involving two AB molecules in the rate-determining step could be found, at the computational level used (see the Supporting Information).

CONCLUSIONS

The results reported herein show that highly active Ir^{III} catalysts have been developed by using the same lutidine-derived CNN^H ligand scaffold with NH amino groups of different basicity. The phenyl-substituted amino complex **4a** in particular is the most active iridium-based catalyst in AB dehydrogenation to date, to the best of our knowledge. The excellent catalytic activity of **4a** is attributed to the formation of a doubly deprotonated species (the amido iridate **5**) upon reaction with a 2-fold excess of *t*BuOK under catalytic conditions. Meanwhile, double deprotonation of Ir-CNN^H complexes based on *N*-alkyl substituted ligands like **4b** cannot be achieved, likely due to the reduced acidity of their amino group. Finally, density functional theory (DFT) calculations of the mechanisms of the first H_2 release from AB catalyzed by **5** reveal that, despite the presence of two Brønsted basic sites (the amido fragment and the methine-NHC arm), the most favorable metal−ligand cooperation mode is based on reversible metal-amine/metal-amido interconversion. Given the widespread use of metal complexes containing proton-responsive ligands in many catalytic processes, this approach, based on the use of ligands with two proton-responsive sites, could lead to improved catalytic systems. Further applications in catalysis of metal complexes incorporating more than one Brønsted acidic/basic sites are currently being explored in our laboratories.

EXPERIMENTAL SECTION

General Procedures. All reactions and manipulations were performed under nitrogen or argon, either in a Braun Labmaster 100 glovebox or using standard Schlenk-type techniques. All solvents were distilled under nitrogen with the following desiccants: sodium-benzophenone-ketyl for diethyl ether (Et_2O) and tetrahydrofuran (THF); sodium for pentane and toluene; CaH_2 for dichloromethane and acetonitrile. Imidazolium salts **1a**−**1c**[25] and Ir(acac)(COD)[35] were prepared as previously described. Deuterated ammonia borane adducts (NH_3BD_3, ND_3BH_3, ND_3BD_3) were synthesized by known methods.[36] All other reagents were purchased from commercial suppliers and used as received. NMR spectra were obtained on Bruker DRX-400 and AVANCEIII/ASCEND 400R spectrometers. $^{11}B\{^1H\}$ NMR shifts were referenced to external $BF_3{\cdot}Et_2O$, while $^{13}C\{^1H\}$ and ^1H shifts were referenced to the residual signals of deuterated solvents. All data are reported in ppm downfield from Me_4Si. All NMR measurements were performed at 25 °C, unless otherwise stated. NMR signal assignations were confirmed by 2D NMR spectroscopy ($^1H-^1H$ COSY, $^1H-^1H$ NOESY, $^1H-^{13}C$ HSQC and $^1H-^{13}C$ HMBC) for all the complexes. Elemental analyses were run by the Analytical Service of the Instituto de Investigaciones Químicas in a Leco TrueSpec CHN elemental analyzer. IR spectra were acquired on a Thermo Scientific Nicolet iS5 iD7 ATR instrument.

Computational Details. Calculations were performed on the real structures of the Ir^{III} anionic complex **5** and the Ir^{III} neutral complex **6** with the Gaussian16[37] package at the DFT//MN15[38] level. Effective core potentials (ECP) and associated SDD basis set[39] supplemented with *f*-polarization functions (SDD(*f*))[40] were used to describe the inner electronic shells and the *d* valence electrons of the Ir atom. All the other atoms were described with a 6-31++G(d,p) basis set.[41] The structures of the reactants and complexes were fully optimized with this basis set without any symmetry restrictions in THF (ε = 7.42), which was introduced within the SMD solvation model.[42] In these optimizations, individual solvation spheres were placed on the H atoms of AB and on the hydride ligands on Ir. The full geometry optimization was followed by the thermochemistry calculations. The nature of all the stationary points on the potential energy surface was confirmed by vibrational analysis. No scaling factors were applied to the calculated frequencies. The transition-state structures showed only one negative eigenvalue in their diagonalized force constant matrices, and their associated eigenvectors were confirmed to correspond to the motion along the reaction coordinate under consideration using the Intrinsic Reaction Coordinate (IRC) method.[43]

https://doi.org/10.1021/acs.inorgchem.1c03056
Inorg. Chem. 2021, 60, 18490−18502

Synthesis of Ir-CNN^H Complexes. *Complex **2a**.* A solution of **1a** (0.105 g, 0.23 mmol) and Ir(acac)(COD) (0.090 g, 0.23 mmol) in CH_2Cl_2 (10 mL) was stirred for 2 days at room temperature. Volatiles were removed under reduced pressure, and the residue was successively washed with pentane (3 × 8 mL) and Et_2O (8 mL), and dried under vacuum. Yellow solid (0.179 g, 99%). Anal. Calcd (%) for $C_{33}H_{38}BrIrN_4$: C 51.96, H 5.02, N 7.34; found: C 51.96, H 4.93, N 7.24. ^{1}H NMR (400 MHz, CD_2Cl_2): δ 7.76 (t, $^3J_{HH}$ = 7.6 Hz, 1H, H arom Py), 7.40 (d, $^3J_{HH}$ = 7.6 Hz, 1H, H arom Py), 7.34 (d, $^3J_{HH}$ = 7.6 Hz, 1H, H arom Py), 7.26 (d, $^3J_{HH}$ = 1.7 Hz, 1H, H arom NHC), 7.19 (dd, $^3J_{HH}$ = 7.3 Hz, $^3J_{HH}$ = 7.3 Hz, 2H, 2 H arom Ph), 7.08 (s, 1H, H arom Mes), 6.98 (s, 1H, H arom Mes), 6.90 (d, $^3J_{HH}$ = 1.7 Hz, 1H, H arom NHC), 6.71 (m, 3H, 3H arom Ph), 6.45 (d, $^2J_{HH}$ = 15.6 Hz, 1H, C*H*H-NHC), 5.58 (d, $^2J_{HH}$ = 15.6 Hz, 1H, CH*H*−NHC), 4.96 (s, 1H, NH), 4.51 (m, 1H, =CH COD), 4.47 (m, 2H, 2 C*H*H−NH), 4.41 (m, 1H, =CH COD), 2.95 (m, 1H, =CH COD), 2.82 (m, 1H, =CH COD), 2.39 (s, 6H, 2 CH_3), 1.95 (s, 3H, CH_3), 1.76 (m, 2H, 2 C*H*H COD), 1.56 (m, 1H, C*H*H COD), 1.38 (m, 4H, 4 C*H*H COD), 1.12 (m, 1H, C*H*H COD). ^{13}C{^{1}H} NMR (101 MHz, CD_2Cl_2): δ 181.0 (C2−NHC), 158.7 (C_q arom), 156.5 (C_q arom), 148.4 (C_q arom), 139.1 (C_q arom), 137.7 (CH arom), 136.9 (C_q arom), 136.3 (C_q arom), 135.1 (C_q arom), 129.7 (CH arom), 129.5 (2 CH arom), 128.5 (CH arom), 123.6 (CH arom), 122.3 (CH arom), 121.2 (CH arom), 120.9 (CH arom), 117.7 (CH arom), 113.3 (2 CH arom), 83.0 (=CH COD), 82.6 (=CH COD), 56.6 (CH_2−NHC), 53.4 (=CH COD), 52.5 (=CH COD), 49.3 (CH_2NH), 34.3 (CH_2 COD), 32.6 (CH_2 COD), 30.0 (CH_2 COD), 29.3 (CH_2 COD), 21.2 (CH_3), 20.3 (CH_3), 18.1 (CH_3).

*Complex **2b**.* A solution of **1b** (0.176 g, 0.40 mmol) and Ir(acac)(COD) (0.159 g, 0.40 mmol) in CH_2Cl_2 (15 mL) was stirred for 24 h at room temperature. Volatiles were removed under reduced pressure, and the residue was washed with pentane (3 × 10 mL) and dried under vacuum. Yellow solid (0.229 g, 77%). Anal. Calcd (%) for $C_{31}H_{42}BrIrN_4$: C 50.12, H 5.70, N 7.54; found: C 49.92, H 5.78, N 7.44. ^{1}H NMR (400 MHz, CD_2Cl_2): δ 7.72 (dd, $^3J_{HH}$ = 7.7 Hz, $^3J_{HH}$ = 7.7 Hz, 1H, H arom Py), 7.34 (m, 2H, 2 H arom Py), 7.23 (d, $^3J_{HH}$ = 1.5 Hz, 1H, H arom NHC), 7.07 (s, 1H, H arom Mes), 6.98 (s, 1H, H arom Mes), 6.86 (d, $^3J_{HH}$ = 1.5 Hz, 1H, H arom NHC), 6.40 (d, $^2J_{HH}$ = 15.7 Hz, 1H, C*H*H−NHC), 5.51 (d, $^2J_{HH}$ = 15.7 Hz, 1H, C*H*H−NHC), 4.49 (m, 1H, =CH COD), 4.41 (m, 1H, =CH COD), 3.89 (m, 2H, 2 C*H*HNH), 3.01 (m, 1H, =CH COD), 2.81 (m, 1H, =CH COD), 2.39 (s, 6H, 2 CH_3), 1.96 (br m, 4H, CH_3 + NH), 1.79 (m, 3H, 3 C*H*H COD), 1.56 (m, 1H, C*H*H COD), 1.43 (m, 1H, C*H*H COD), 1.32 (m, 2H, 2 C*H*H COD), 1.18 (s, 9H, C(CH_3)$_3$), 1.12 (m, 1H, C*H*H COD). ^{13}C{^{1}H} NMR (101 MHz, CD_2Cl_2): δ 180.9 (C2−NHC), 161.5 (C_q arom), 156.1 (C_q arom), 139.1 (C_q arom), 137.5 (CH arom), 136.9 (C_q arom), 136.3 (C_q arom), 135.1 (C_q arom), 129.7 (CH arom), 128.5 (CH arom), 123.6 (CH arom), 122.2 (CH arom), 121.5 (CH arom), 120.7 (CH arom), 82.9 (=CH COD), 82.5 (=CH COD), 56.7 (CH_2−NHC), 52.4 (2 =CH COD), 50.7 (C(CH_3)$_3$), 48.8 (CH_2NH), 34.3 (CH_2 COD), 32.6 (CH_2 COD), 30.1 (CH_2 COD), 29.3 (C(CH_3)$_3$ + CH_2 COD), 21.2 (CH_3), 20.3 (CH_3), 18.1 (CH_3).

*Complex **3**.* A solution of Ir(acac)(COD) (0.059 g, 0.15 mmol) in CH_2Cl_2 (10 mL) was added to a solution of **1c** (0.070 g, 0.15 mmol) in CH_2Cl_2 (10 mL). The mixture was stirred at room temperature for 24 h, and at 50 °C for 36 h. Solvent was removed under reduced pressure, and the residue was washed with MeCN (2 × 7 mL) and dried under vacuum. Yellow solid (0.024 g, 24%). Anal. Calcd (%) for $C_{26}H_{28}BrIrN_4$: C 46.70, H 4.22, N 8.38; found: C 46.80, H 4.53, N 8.81. ^{1}H NMR (400 MHz, CD_2Cl_2): δ 7.68 (dd, $^3J_{HH}$ = 7.9 Hz, $^3J_{HH}$ = 7.9 Hz, 1H, H arom Py), 7.30 (d, $^3J_{HH}$ = 7.9 Hz, 1H, H arom Py), 7.28 (d, $^3J_{HH}$ = 2.2 Hz, 1H, H arom NHC), 7.15 (d, $^3J_{HH}$ = 7.9 Hz, 1H, H arom Py), 6.99 (s, 1H, H arom Mes), 6.98 (d, $^3J_{HH}$ = 2.2 Hz, 1H, H arom NHC), 6.90 (s, 1H, H arom Mes), 6.79 (d, $^3J_{HH}$ = 7.7 Hz, 1H, H arom Ph), 6.72 (dd, $^3J_{HH}$ = 7.7 Hz, $^4J_{HH}$ = 1.2 Hz, 1H, H arom Ph), 6.61 (ddd, $^3J_{HH}$ = 7.3 Hz, $^3J_{HH}$ = 7.3 Hz, $^4J_{HH}$ = 1.2 Hz, 1H, H arom Ph), 6.53 (dd, $^3J_{HH}$ = 7.3 Hz, $^3J_{HH}$ = 7.3 Hz, 1H, H arom Ph), 5.78 (d, $^2J_{HH}$ = 16.0 Hz, 1H, C*H*H−NHC), 5.41 (d, $^2J_{HH}$ = 16.1 Hz, 1H, C*H*H−NHC), 5.26 (m, 2H, C*H*HNH + NH), 4.50 (dd, $^2J_{HH}$ = 15.3 Hz, $^3J_{HH}$ = 7.1 Hz, 1H, C*H*HN), 4.15 (d, $^2J_{HH}$ = 16.1 Hz, 1H, C*H*HNH), 3.92 (d, $^2J_{HH}$ = 15.3 Hz, 1H, C*H*HNH), 2.35 (s, 3H, CH_3), 2.30 (s, 3H, CH_3), 2.10 (s, 3H, CH_3), −17.73 (s, 1H, IrH). ^{13}C{^{1}H} NMR (101 MHz, CD_2Cl_2): δ 162.8 (C_q arom), 161.3 (C2−NHC), 150.8 ($C_q$arom), 148.2 ($C_q$arom), 140.0 (Ir−$C_q$arom), 138.2 ($C_q$arom), 138.1 ($C_q$arom), 137.7 (CHarom), 137.1 ($C_q$arom), 136.5 (CHarom), 136.4 ($C_q$arom), 129.4 (CH arom), 128.6 (CH arom), 124.9 (CH arom), 121.8 (CH arom), 121.7 (CH arom), 120.9 (CH arom), 120.9 (CH arom), 120.7 (CH arom), 120.2 (CH arom), 66.5 (CH_2NH), 64.2 (CH_2NH), 55.3 (CH_2−NHC), 21.3 (CH_3), 20.1 (CH_3), 19.7 (CH_3).

*Complex **4a**.* In a Fisher−Porter vessel, a solution of **2a** (0.172 g, 0.22 mmol) in CH_2Cl_2 (8 mL) was pressurized with 5 bar of H_2 and stirred for 24 h at room temperature. The system was depressurized, solvent was evaporated, and the residue was washed with pentane (2 × 8 mL) cooled to −30 °C and dried. Yellow solid (0.043 g, 29%). Anal. Calcd (%) for $C_{25}H_{28}BrIrN_4$: C, 45.73; H, 4.30; N, 8.53; found: C, 45.41; H, 4.47; N, 8.21. ^{1}H NMR (400 MHz, CD_2Cl_2): δ 7.86 (dd, $^3J_{HH}$ = 7.7 Hz, $^3J_{HH}$ = 7.7 Hz, 1H, H arom Py), 7.46 (dd, $^3J_{HH}$ = 7.2 Hz, $^3J_{HH}$ = 7.2 Hz, 2H, 2 H arom Ph), 7.33 (m, 4H, 4 H arom), 7.14 (m, 2H, 2 H arom), 6.96 (m, 2H, 2 H arom), 6.72 (d, $^3J_{HH}$ = 1.8 Hz, 1H, H arom NHC), 6.41 (d, $^2J_{HH}$ = 15.0 Hz, 1H, C*H*H−NHC), 6.15 (br d, $^3J_{HH}$ = 11.1 Hz, 1H, NH), 5.05 (d, $^2J_{HH}$ = 15.0 Hz, 1H, CH*H*−NHC), 4.76 (dd, $^2J_{HH}$ = 14.5 Hz, $^3J_{HH}$ = 2.8 Hz, 1H, C*H*H−NH), 4.62 (d, $^2J_{HH}$ = 14.5 Hz, $^3J_{HH}$ = 11.1 Hz, 1H, CH*H*−NH), 2.34 (s, 3H, CH_3), 2.14 (s, 3H, CH_3), 1.92 (s, 3H, CH_3), −19.05 (d, $^2J_{HH}$ = 6.9 Hz, 1H, IrH *trans* to Py), −23.25 (d, $^2J_{HH}$ = 6.9 Hz, 1H, IrH *cis* to Py). ^{13}C{^{1}H} NMR (101 MHz, CD_2Cl_2): δ 159.8 (C_q arom), 153.5 (C2−NHC), 149.5 (C_q arom), 138.0 (C_q arom), 137.5 (C_q arom), 136.5 (C_q arom), 135.6 (CH arom), 135.0 (C_q arom), 128.9 (2 CH arom + C_q arom), 128.7 (CH arom), 128.3 (CH arom), 125.0 (CH arom), 122.8 (CH arom), 120.9 (CH arom), 120.5 (CH arom), 120.1 (2 CH arom), 119.3 (CH arom), 62.2 (CH_2NH), 55.3 (CH_2−NHC), 20.9 (CH_3), 18.8 (CH_3), 17.9 (CH_3).

*Complex **4b**.* This complex was prepared as described above for **4a**. Yellow solid (0.084 g, 40%). Anal. Calcd (%) for $C_{23}H_{32}BrIrN_4$: C 43.39, H 5.07, N 8.80; found: C 43.50, H 5.14, N 8.42. ^{1}H NMR (400 MHz, CD_2Cl_2): δ 7.77 (dd, $^3J_{HH}$ = 7.7 Hz, $^3J_{HH}$ = 7.7 Hz, 1H, H arom Py), 7.37 (d, $^3J_{HH}$ = 7.7 Hz, 1H, H arom Py), 7.36 (d, $^3J_{HH}$ = 7.7 Hz, 1H, H arom Py), 7.12 (d, $^3J_{HH}$ = 2.1 Hz, 1H, H arom NHC), 7.03 (s, 1H, H arom Mes), 6.96 (s, 1H, H arom Mes), 6.71 (d, $^3J_{HH}$ = 2.1 Hz, 1H, H arom NHC), 6.43 (d, $^2J_{HH}$ = 14.9 Hz, 1H, C*H*H−NHC), 4.98 (d, $^2J_{HH}$ = 14.9 Hz, 1H, C*H*H−NHC), 4.53 (dd, $^2J_{HH}$ = 13.5 Hz, $^3J_{HH}$ = 3.2 Hz, 1H, C*H*HNH), 4.03 (br dd, $^3J_{HH}$ = 12.5 Hz, $^3J_{HH}$ = 3.2 Hz, 1H, NH), 3.91 (dd, $^2J_{HH}$ = 13.5 Hz, $^3J_{HH}$ = 12.5 Hz, 1H, C*H*HNH), 2.39 (s, 3H, CH_3), 2.18 (s, 3H, CH_3), 1.94 (s, 3H, CH_3), 1.33 (s, 9H, C(CH_3)$_3$), −19.02 (d, 1H, $^2J_{HH}$ = 7.1 Hz, IrH *trans* to Py), −23.92 (d, 1H, $^2J_{HH}$ = 7.1 Hz, IrH *cis* to Py). ^{13}C{^{1}H} NMR (101 MHz, CD_2Cl_2): δ 162.4 (C_q arom), 156.9 (C2−NHC), 153.7 (C_q arom), 138.3 (C_q arom), 138.0 (C_q arom), 137.0 (C_q arom), 135.5 (C_q arom), 135.4 (CH arom), 128.9 (CH arom), 128.5 (CH arom), 122.7 (CH arom), 120.9 (CH arom), 120.6 (CH arom), 119.5 (CH arom), 56.3 (CH_2NH + C(CH_3)$_3$), 55.7 (CH_2−NHC), 28.8 (C(CH_3)$_3$), 21.3 (CH_3), 19.2 (CH_3), 18.4 (CH_3).

*Complex **4c**.* In a Fisher−Porter vessel, a suspension of complex **3** (0.040 g, 0.06 mmol) in CH_2Cl_2 (5 mL) was pressurized with 4 bar of H_2, and stirred at 60 °C for 24 h. The system was depressurized, solvent was evaporated and the residue was washed with and pentane (2 × 8 mL), and dried. Yellow solid (0.039 g, 97%). Anal. Calcd (%) for $C_{26}H_{30}BrIrN_4$: C, 46.56; H, 4.51; N, 8.35; found: C, 46.46; H, 4.84; N, 8.17. ^{1}H NMR (400 MHz, CD_2Cl_2): δ 7.72 (dd, $^3J_{HH}$ = 7.4 Hz, $^3J_{HH}$ = 7.4 Hz, 1H, H arom Py), 7.38 (m, 7H, 7 H arom), 7.20 (d, $^3J_{HH}$ = 7.4 Hz, 1H, H arom Py), 7.16 (s, 1H, H arom), 7.05 (s, 1H, H arom), 7.00 (s, 1H, H arom), 6.35 (d, $^2J_{HH}$ = 15.0 Hz, 1H, C*H*H−NHC), 5.05 (d, $^2J_{HH}$ = 15.0 Hz, 1H, C*H*H−NHC), 4.78 (d, $^2J_{HH}$ = 13.9 Hz, 1H, C*H*HNH), 4.39 (br dd, $^3J_{HH}$ = 9.2 Hz, $^3J_{HH}$ = 9.2 Hz, 1H, NH), 4.28 (dd, $^2J_{HH}$ = 15.0 Hz, $^3J_{HH}$ = 3.1 Hz, 1H, C*H*HNH), 3.92 (dd, $^2J_{HH}$ = 13.3 Hz, $^3J_{HH}$ = 12.9 Hz, 1H, C*H*HNH), 3.73 (dd, $^2J_{HH}$ = 13.6 Hz, $^3J_{HH}$ = 12.9 Hz, 1H, C*H*HNH), 2.40 (s, 3H, CH_3),

https://doi.org/10.1021/acs.inorgchem.1c03056
Inorg. Chem. 2021, 60, 18490−18502

2.22 (s, 3H, CH_3), 1.96 (s, 3H, CH_3), −18.83 (d, 1H, $^2J_{HH}$ = 6.9 Hz, IrH *trans* to Py), −23.28 (d, 1H, $^2J_{HH}$ = 6.9 Hz, IrH *cis* to Py). $^{13}C\{^1H\}$ NMR (101 MHz, CD_2Cl_2): δ 161.0 (C_q arom), 156.8 (C2−NHC), 153.3 (C_q arom), 138.1 (C_q arom), 137.9 (C_q arom), 136.9 (C_q arom), 135.2 (CH arom), 135.0 (C_q arom), 129.0 (2 CH arom), 128.8 (3 CH arom), 128.2 (CH arom), 128.0 (CH arom), 122.4 (CH arom), 120.7 (CH arom), 120.2 (CH arom), 119.1 (CH arom), 63.9 (CH_2NH), 60.3 (CH_2NH), 55.4 (CH_2−NHC), 20.9 (CH_3), 18.9 (CH_3), 18.0 (CH_3).

Complex ***5***. In a J. Young-valved NMR tube, a suspension of complex **4a** (0.014 g, 0.02 mmol) in THF-d_8 (0.5 mL) was treated with *t*BuOK (0.005 g, 0.04 mmol). The sample was analyzed by NMR spectroscopy, showing the formation of complex **5** in ca. 90% NMR yield. Crystals of **5** suitable for XRD analysis were obtained by cooling the above solution at −30 °C. ^1H NMR (400 MHz, THF-d_8): δ 7.15 (d, $^3J_{HH}$ = 8.6 Hz, 1H, H arom), 6.97 (d, $^3J_{HH}$ = 5.1 Hz, 2H, 2 H arom), 7.73 (m, 4H, 4 H arom), 6.41 (s, 1H, H arom), 6.25 (s, 1H, CH−NHC), 6.06 (d, $^3J_{HH}$ = 7.6 Hz, 2H, 2 H arom), 5.75 (m, 2H, 2 H arom), 4.24 (d, $^2J_{HH}$ = 16.5 Hz, 1H, C*H*H−NPh), 3.80 (d, $^2J_{HH}$ = 16.5 Hz, 1H, C*H*H−NPh), 2.29 (s, 3H, CH_3), 2.21 (s, 3H, CH_3), 1.77 (overlapped with solvent signal, CH_3), −16.35 (d, $^2J_{HH}$ = 5.5 Hz, 1H, IrH), −18.61 (d, $^2J_{HH}$ = 5.5 Hz, 1H, IrH). $^{13}C\{^1H\}$ NMR (101 MHz, THF-d_8): δ 164.4 (C_q arom), 164.0 (C_q arom), 159.0 (C_q arom), 156.8 (C2−NHC), 142.3 (C_q arom), 138.7 (C_q arom), 138.4 (C_q arom), 136.3 (C_q arom), 129.8 (CH arom), 129.0 (CH arom), 128.8 (CH arom), 128.3 (CH arom), 127.6 (CH arom), 120.0 (CH arom), 119.8 (CH arom), 116.7 (CH arom), 114.5 (CH arom), 108.3 (CH arom), 107.1 (CH arom), 105.4 (CH arom), 64.2 (CH_2N), 49.0 (CH−NHC), 21.0 (CH_3), 20.9 (CH_3), 20.1 (CH_3).

Complex ***6***. In a J. Young-valved NMR tube, a suspension of complex **4b** (0.015 g, 0.02 mmol) in THF-d_8 (0.5 mL) was treated with *t*BuOK (0.007 g, 0.06 mmol). The sample was analyzed by NMR spectroscopy, showing the formation of complex **6** in 75%−80% NMR yield. ^1H NMR (400 MHz, THF-d_8): δ 7.29 (dd, $^3J_{HH}$ = 7.5 Hz, $^3J_{HH}$ = 7.5 Hz, 1H, H arom Py), 6.81 (s, 1H, H arom Mes), 6.80 (d, $^3J_{HH}$ = 1.6 Hz, 1H, H arom NHC), 6.72 (s, 1H, H arom Mes), 6.31 (d, $^3J_{HH}$ = 1.6 Hz, 1H, H arom NHC), 6.16 (d, $^3J_{HH}$ = 7.3 Hz, 1H, H arom Py), 5.95 (d, $^3J_{HH}$ = 7.6 Hz, 1H, H arom Py), 5.48 (s,1H, NHC−CH), 3.88 (dd, $^2J_{HH}$ = 13.6 Hz, $^3J_{HH}$ = 2.8 Hz, 1H, C*H*HN), 3.39 (m, 1H, C*H*HN), 2.97 (br d, $^2J_{HH}$ = 10.9 Hz, 1H, NH), 2.25 (s, 3H, CH_3), 2.04 (s, 3H, CH_3), 1.77 (s, 3H, CH_3), 1.31 (s, 9H, $C(CH_3)_3$), − 16.49 (d, $^2J_{HH}$ = 5.6 Hz, 1H, IrH), −18.41 (d, $^2J_{HH}$ = 5.6 Hz, 1H, IrH). $^{13}C\{^1H\}$ NMR (101 MHz, THF-d_8): δ 164.5 ($C_q$arom), 161.5 ($C_q$arom), 150.0 (C2−NHC), 140.6 ($C_q$arom), 137.5 ($C_q$arom), 136.3 ($C_q$arom), 136.1 ($C_q$arom), 131.1 (CH arom), 128.4 (CH arom), 127.9 (CH arom), 120.0 (CH arom), 116.4 (CH arom), 112.5 (CH arom), 110.2 (CH arom), 56.8 ($C(CH_3)_3$), 56.1 (CH_2NH), 54.9 (CH−NHC), 29.2 ($C(CH_3)_3$), 21.1 (CH_3), 20.8 (CH_3), 20.0 (CH_3).

Complex ***7***. In a J. Young-valved NMR tube, a suspension of complex **4b** (0.015 g, 0.02 mmol) in THF-d_8 (0.5 mL) was treated with *t*BuOK (0.007 g, 0.06 mmol). The sample was pressurized with 4 bar H_2, and analyzed by NMR spectroscopy after 48 h. ^1H NMR (400 MHz, THF-d_8): δ 7.52 (dd, $^3J_{HH}$ = 7.6 Hz, $^3J_{HH}$ = 7.6 Hz, 1H, H arom Py), 7.15 (m, 2H, 2 H arom Py), 7.00 (d, $^3J_{HH}$ = 1.9 Hz, 1H, H arom NHC), 6.82 (s, 1H, H arom Mes), 6.80 (s, 1H, H arom Mes), 6.56 (d, $^3J_{HH}$ = 1.9 Hz, 1H, H arom NHC), 5.10 (d, $^2J_{HH}$ = 13.5 Hz,1H, C*H*H−NHC), 5.02 (br, 1H, NH), 5.02 (d, $^2J_{HH}$ = 13.5 Hz,1H, C*H*H-NHC), 4.25 (dd, $^2J_{HH}$ = 14.4 Hz, $^3J_{HH}$ = 3.8 Hz, 1H, C*H*HN), 4.02 (dd, $^2J_{HH}$ = 14.4 Hz, $^3J_{HH}$ = 5.8 Hz, 1H, C*H*HN), 2.27 (s, 3H, CH_3), 2.03 (s, 3H, CH_3), 1.95 (s, 3H, CH_3), 1.11 (s, 9H, $C(CH_3)_3$), −8.92 (m, 2H, 2 IrH), −18.24 (dd, $^2J_{HH}$ = 5.2 Hz, $^2J_{HH}$ = 5.2 Hz, 1H, IrH). $^{13}C\{^1H\}$ NMR (101 MHz, THF-d_8): δ 164.5 ($C_q$arom), 164.0 ($C_q$arom), 153.8 (C2−NHC), 139.5 ($C_q$arom), 137.3 ($C_q$arom), 136.7 ($C_q$arom), 131.5 (CH arom), 128.6 (CH arom), 128.5 (CH arom), 120.9 (CH arom), 119.1 (CH arom), 118.6 (CH arom), 117.9 (CH arom), 59.0 (CH_2−NHC), 57.7 (CH_2NH), 50.7 ($C(CH_3)_3$), 27.5 ($C(CH_3)_3$), 21.1 (CH_3), 19.6 (CH_3), 19.4 (CH_3); signals of two quaternary aromatic carbons could not be unambiguously assigned.

Ammonia-Borane Dehydrogenation. *Experimental Setup for H_2 Production.* H_2 generation was followed up using a Fisher-Porter vessel (25 mL) that was connected to a vacuum line and coupled to an ESI pressure gauge model GS4200-USB (0−6 bar) that was connected to a computer (see the Supporting Information for details).

Representative Procedure for AB Dehydrogenation. A solution of complex **4a** (4.3 mg, 6.5 μmol) and *t*BuOK (1.8 mg, 0.016 mmol) in THF (0.5 mL) was added to a freshly prepared, stirred (750 rpm) solution of AB (50.0 mg, 1.62 mmol) in THF (0.5 mL) at room temperature. H_2 generation was monitored by registering the increase of pressure in the system. At the end of the reaction, the supernatant was transferred to an NMR tube and analyzed via ^{11}B NMR spectroscopy, to identify the soluble reaction byproducts. The insoluble residue was washed subsequently with THF and Et_2O, and then dried under vacuum before recording the IR spectrum.

■ ASSOCIATED CONTENT

Supporting Information

The Supporting Information is available free of charge at https://pubs.acs.org/doi/10.1021/acs.inorgchem.1c03056.

Experimental setup details, kinetic studies, selected NMR spectra, and X-ray diffraction data (PDF)

Cartesian coordinates, absolute Gibbs energies (THF) and imaginary frequencies (TSs) of the DFT-optimized structures (XYZ)

Accession Codes

CCDC 2113023−2113025 contain the supplementary crystallographic data for this paper. These data can be obtained free of charge via www.ccdc.cam.ac.uk/data_request/cif, or by emailing data_request@ccdc.cam.ac.uk, or by contacting The Cambridge Crystallographic Data Centre, 12 Union Road, 909 Cambridge CB2 1EZ, UK; fax: + 44 1223 336033.

■ AUTHOR INFORMATION

Corresponding Authors

Andrea Rossin − *Istituto di Chimica dei Composti Organometallici - Consiglio Nazionale delle Ricerche (ICCOM - CNR), 50019 Sesto, Fiorentino, Italy*; Email: a.rossin@iccom.cnr.it

Andrés Suárez − *Instituto de Investigaciones Químicas (IIQ), Departamento de Química Inorgánica and Centro de Innovación en Química Avanzada (ORFEO−CINQA), CSIC and Universidad de Sevilla, 41092 Sevilla, Spain*; orcid.org/0000-0002-0487-611X; Email: andres.suarez@iiq.csic.es

Authors

Isabel Ortega-Lepe − *Instituto de Investigaciones Químicas (IIQ), Departamento de Química Inorgánica and Centro de Innovación en Química Avanzada (ORFEO−CINQA), CSIC and Universidad de Sevilla, 41092 Sevilla, Spain*

Práxedes Sánchez − *Instituto de Investigaciones Químicas (IIQ), Departamento de Química Inorgánica and Centro de Innovación en Química Avanzada (ORFEO−CINQA), CSIC and Universidad de Sevilla, 41092 Sevilla, Spain*

Laura L. Santos − *Instituto de Investigaciones Químicas (IIQ), Departamento de Química Inorgánica and Centro de Innovación en Química Avanzada (ORFEO−CINQA), CSIC and Universidad de Sevilla, 41092 Sevilla, Spain*

Nuria Rendón − *Instituto de Investigaciones Químicas (IIQ), Departamento de Química Inorgánica and Centro de Innovación en Química Avanzada (ORFEO−CINQA), CSIC and Universidad de Sevilla, 41092 Sevilla, Spain*; orcid.org/0000-0003-1760-185X

Eleuterio Álvarez − *Instituto de Investigaciones Químicas (IIQ), Departamento de Química Inorgánica and Centro de Innovación en Química Avanzada (ORFEO−CINQA), CSIC and Universidad de Sevilla, 41092 Sevilla, Spain*

Joaquín López-Serrano − *Instituto de Investigaciones Químicas (IIQ), Departamento de Química Inorgánica and Centro de Innovación en Química Avanzada (ORFEO−CINQA), CSIC and Universidad de Sevilla, 41092 Sevilla, Spain;* orcid.org/0000-0003-3999-0155

Complete contact information is available at: https://pubs.acs.org/10.1021/acs.inorgchem.1c03056

Notes

The authors declare no competing financial interest.

■ ACKNOWLEDGMENTS

Financial support (FEDER contribution) from the Spanish Agencia Estatal de Investigación (PID2019-104159GB-I00/AEI/10.13039/501100011033) and Junta de Andalucía (P18-FR-3208) is gratefully acknowledged. A.R. would like to thank the CNR-RFBR (Russia) Bilateral Project (2018-2020) for financial support to this research activity. Mr. Arne Estelmann is thanked for preliminary experimental work.

■ REFERENCES

(1) (a) Yadav, M.; Xu, Q. Liquid-Phase Chemical Hydrogen Storage Materials. *Energy Environ. Sci.* **2012**, *5*, 9698−9725. (b) Dalebrook, A. F.; Gan, W.; Grasemann, M.; Moret, S.; Laurenczy, G. Hydrogen Storage: Beyond Conventional Methods. *Chem. Commun.* **2013**, *49*, 8735−8751. (c) Demirci, U. B.; Miele, P. Chemical Hydrogen Storage: 'Material' Gravimetric Capacity versus 'System' Gravimetric Capacity. *Energy Environ. Sci.* **2011**, *4*, 3334−3341.

(2) (a) Durbin, D. J.; Malardier-Jugroot, C. Review of Hydrogen Storage Techniques for On Board Vehicle Applications. *Int. J. Hydrogen Energy* **2013**, *38*, 14595−14617. (b) Zhang, F.; Zhao, P.; Niu, M.; Maddy, J. The Survey of Key Technologies in Hydrogen Energy Storage. *Int. J. Hydrogen Energy* **2016**, *41*, 14535−14552. (c) Sakintuna, B.; Lamari-Darkrim, F.; Hirscher, M. Metal Hydride Materials for Solid Hydrogen Storage: A Review. *Int. J. Hydrogen Energy* **2007**, *32*, 1121−1140.

(3) (a) Stephens, F. H.; Pons, V.; Tom Baker, R. Ammonia−Borane: The Hydrogen Source Par Excellence? *Dalton Trans.* **2007**, 2613−2626. (b) Hamilton, C. W.; Baker, R. T.; Staubitz, A.; Manners, I. B−N Compounds for Chemical Hydrogen Storage. *Chem. Soc. Rev.* **2009**, *38*, 279−293. (c) Staubitz, A.; Robertson, A. P. M.; Manners, I. Ammonia-Borane and Related Compounds as Dihydrogen Sources. *Chem. Rev.* **2010**, *110*, 4079−4124. (d) Li, H.; Yang, Q.; Chen, X.; Shore, S. G. Ammonia Borane, Past as Prolog. *J. Organomet. Chem.* **2014**, *751*, 60−66. (e) Marder, T. B. Will We Soon Be Fueling our Automobiles with Ammonia-Borane? *Angew. Chem., Int. Ed.* **2007**, *46*, 8116−8118.

(4) (a) Staubitz, A.; Presa Soto, A.; Manners, I. Iridium-Catalyzed Dehydrocoupling of Primary Amine−Borane Adducts: A Route to High Molecular Weight Polyaminoboranes, Boron−Nitrogen Analogues of Polyolefins. *Angew. Chem., Int. Ed.* **2008**, *47*, 6212−6215. (b) Clark, T. J.; Lee, K.; Manners, I. Transition-Metal-Catalyzed Dehydrocoupling: A Convenient Route to Bonds between Main-Group Elements. *Chem. - Eur. J.* **2006**, *12*, 8634−8648. (c) Staubitz, A.; Robertson, A. P. M.; Sloan, M. E.; Manners, I. Amine- and Phosphine-Borane Adducts: New Interest in Old Molecules. *Chem. Rev.* **2010**, *110*, 4023−4078. (d) Whittell, G. R.; Manners, I. Advances with Ammonia-Borane: Improved Recycling and Use as a Precursor to Atomically Thin BN Films. *Angew. Chem., Int. Ed.* **2011**, *50*, 10288−10289. (e) Colebatch, A. L.; Weller, A. S. Amine−Borane Dehydropolymerization:Challenges andOpportunities. *Chem. - Eur. J.* **2019**, *25*, 1379−1390. (f) Han, D.; Anke, F.; Trose, M.; Beweries, T. Recent Advances in Transition Metal Catalysed Dehydropolymerisation of Amine Boranes and Phosphine Boranes. *Coord. Chem. Rev.* **2019**, *380*, 260−286.

(5) (a) Smythe, N. C.; Gordon, J. C. Ammonia Borane as a Hydrogen Carrier: Dehydrogenation and Regeneration. *Eur. J. Inorg. Chem.* **2010**, *2010*, 509−521. (b) Bluhm, M. E.; Bradley, M. G.; Butterick, R., III; Kusari, U.; Sneddon, L. G. Amineborane-Based Chemical Hydrogen Storage: Enhanced Ammonia Borane Dehydrogenation in Ionic Liquids. *J. Am. Chem. Soc.* **2006**, *128*, 7748−7749.

(6) (a) Rossin, A.; Peruzzini, M. Ammonia-Borane and Amine-Borane Dehydrogenation Mediated by Complex Metal Hydrides. *Chem. Rev.* **2016**, *116*, 8848−8872. (b) Alcaraz, G.; Sabo-Etienne, S. Coordination and Dehydrogenation of Amine−Boranes at Metal Centers. *Angew. Chem., Int. Ed.* **2010**, *49*, 7170−7179. (c) Bhunya, S.; Malakar, T.; Ganguly, G.; Paul, A. Combining Protons and Hydrides by Homogeneous Catalysis for Controlling the Release of Hydrogen from Ammonia-Borane: Present Status and Challenges. *ACS Catal.* **2016**, *6*, 7907−7934.

(7) Denney, M. C.; Pons, V.; Hebden, T. J.; Heinekey, D. M.; Goldberg, K. I. Efficient Catalysis of Ammonia Borane Dehydrogenation. *J. Am. Chem. Soc.* **2006**, *128*, 12048−12049.

(8) Bhattacharya, P.; Krause, J. A.; Guan, H. Mechanistic Studies of Ammonia Borane Dehydrogenation Catalyzed by Iron Pincer Complexes. *J. Am. Chem. Soc.* **2014**, *136*, 11153−11161.

(9) Nugent, J. W.; García-Melchor, M.; Fout, A. R. Cobalt-Catalyzed Ammonia Borane Dehydrogenation: Mechanistic Insight and Isolation of a Cobalt Hydride-Amidoborane Complex. *Organometallics* **2020**, *39*, 2917−2927.

(10) Esteruelas, M. A.; Nolis, P.; Oliván, M.; Oñate, E.; Vallribera, A.; Vélez, A. Ammonia Borane Dehydrogenation Promoted by a Pincer-Square-Planar Rhodium(I) Monohydride: A Stepwise Hydrogen Transfer from the Substrate to the Catalyst. *Inorg. Chem.* **2016**, *55*, 7176−7181.

(11) Luconi, L.; Osipova, E. S.; Giambastiani, G.; Peruzzini, M.; Rossin, A.; Belkova, N. V.; Filippov, O. A.; Titova, E. M.; Pavlov, A. A.; Shubina, E. S. Amine Boranes Dehydrogenation Mediated by an Unsymmetrical Iridium Pincer Hydride: (PCN) vs (PCP) Improved Catalytic Performance. *Organometallics* **2018**, *37*, 3142−3153.

(12) Rossin, A.; Bottari, G.; Lozano-Vila, A. M.; Paneque, M.; Peruzzini, M.; Rossi, A.; Zanobini, F. Catalytic Amine-Borane Dehydrogenation by a PCP-Pincer Palladium Complex: A Combined Experimental and DFT Analysis of the Reaction Mechanism. *Dalton Trans.* **2013**, *42*, 3533−3541.

(13) (a) Käβ, M.; Friedrich, A.; Drees, M.; Schneider, S. Ruthenium Complexes with Cooperative PNP Ligands: Bifunctional Catalysts for the Dehydrogenation of Ammonia-Borane. *Angew. Chem., Int. Ed.* **2009**, *48*, 905−907. (b) Marziale, A. N.; Friedrich, A.; Klopsch, I.; Drees, M.; Celinski, V. R.; Schmedt auf der Günne, J.; Schneider, S. The Mechanism of Borane-Amine Dehydrocoupling with Bifunctional Ruthenium Catalysts. *J. Am. Chem. Soc.* **2013**, *135*, 13342−13355.

(14) Glüer, A.; Förster, M.; Celinski, V. R.; Schmedt auf der Günne, J.; Holthausen, M. C.; Schneider, S. Highly Active Iron Catalyst for Ammonia Borane Dehydrocoupling at Room Temperature. *ACS Catal.* **2015**, *5*, 7214−7217.

(15) Elsby, M. R.; Ghostine, K.; Das, U. K.; Gabidullin, B. M.; Baker, R. T. Iron-SNS and -CNS Complexes: Selective C_{aryl}-S Bond Cleavage and Amine-Borane Dehydrogenation Catalysis. *Organometallics* **2019**, *38*, 3844−3851.

(16) Luconi, L.; Demirci, U. B.; Peruzzini, M.; Giambastiani, G.; Rossin, A. Ammonia Borane and Hydrazine Bis(Borane) Dehydrogenation Mediated by an Unsymmetrical (PNN) Ruthenium Pincer Hydride: Metal−Ligand Cooperation for Hydrogen Production. *Sustainable Energy Fuels* **2019**, *3*, 2583−2596.

(17) Blaquiere, N.; Diallo-Garcia, S.; Gorelsky, S. I.; Black, D. A.; Fagnou, K. Ruthenium-Catalyzed Dehydrogenation of Ammonia Boranes. *J. Am. Chem. Soc.* **2008**, *130*, 14034−14035.

(18) Takahashi, H.; Watanabe, T.; Tobita, H. Bifunctional Iron-Amino Complexes: Highly Efficient Catalysts for Dehydrogenation of Ammonia-Borane. *Chem. Lett.* **2018**, *47*, 296−299.

(19) (a) Conley, B. L.; Williams, T. J. Dehydrogenation of Ammonia-Borane by Shvo's Catalyst. *Chem. Commun.* **2010**, *46*, 4815−4817. (b) Conley, B. L.; Guess, D.; Williams, T. J. A Robust, Air-Stable, Reusable Ruthenium Catalyst for Dehydrogenation of Ammonia Borane. *J. Am. Chem. Soc.* **2011**, *133*, 14212−14215.
(20) (a) Zhao, B.; Han, Z.; Ding, K. The N-H Functional Group in Organometallic Catalysis. *Angew. Chem., Int. Ed.* **2013**, *52*, 4744−4788. (b) Dub, P. A.; Gordon, J. C. The Role of the Metal-Bound N−H Functionality in Noyori-Type Molecular Catalysts. *Nat. Rev. Chem.* **2018**, *2*, 396−408.
(21) (a) Milstein, D. Metal-Ligand Cooperation by Aromatization-Dearomatization as a Tool in Single Bond Activation. *Philos. Trans. R. Soc., A* **2015**, *373*, 20140189. (b) Shimbayashi, T.; Fujita, K. Recent Advances in Homogeneous Catalysis via Metal-Ligand Cooperation Involving Aromatization and Dearomatization. *Catalysts* **2020**, *10*, 635.
(22) (a) Filonenko, G. A.; Cosimi, E.; Lefort, L.; Conley, M. P.; Copéret, C.; Lutz, M.; Hensen, E. J. M.; Pidko, E. A. Lutidine-Derived Ru-CNC Hydrogenation Pincer Catalysts with Versatile Coordination Properties. *ACS Catal.* **2014**, *4*, 2667−2671. (b) Filonenko, G. A.; Smykowski, D.; Szyja, B. M.; Li, G.; Szczygiel, J.; Hensen, E. J. M.; Pidko, E. A. Catalytic Hydrogenation of CO_2 to Formates by a Lutidine-Derived Ru-CNC Pincer Complex: Theoretical Insight into the Unrealized Potential. *ACS Catal.* **2015**, *5*, 1145−1154. (c) Sun, Y.; Koehler, C.; Tan, R.; Annibale, V. T.; Song, D. Ester Hydrogenation Catalyzed by Ru-CNN Pincer Complexes. *Chem. Commun.* **2011**, *47*, 8349−8351. (d) Del Pozo, C.; Iglesias, M.; Sánchez, F. Pincer-Type Pyridine-Based N-Heterocyclic Carbene Amine Ru(II) Complexes as Efficient Catalysts for Hydrogen Transfer Reactions. *Organometallics* **2011**, *30*, 2180−2188. (e) Fogler, E.; Balaraman, E.; Ben-David, Y.; Leitus, G.; Shimon, L. J. W.; Milstein, D. New CNN-Type Ruthenium Pincer NHC Complexes. Mild, Efficient Catalytic Hydrogenation of Esters. *Organometallics* **2011**, *30*, 3826−3833. (f) Hernández-Juárez, M.; Vaquero, M.; Álvarez, E.; Salazar, V.; Suárez, A. Hydrogenation of Imines Catalysed by Ruthenium(II) Complexes Based on Lutidine-Derived CNC Pincer Ligands. *Dalton Trans.* **2013**, *42*, 351−354. (g) Hernández-Juárez, M.; López-Serrano, J.; Lara, P.; Morales-Cerón, J. P.; Vaquero, M.; Álvarez, E.; Salazar, V.; Suárez, A. Ruthenium(II) Complexes Containing Lutidine-Derived Pincer CNC Ligands: Synthesis, Structure, and Catalytic Hydrogenation of C-N Bonds. *Chem. - Eur. J.* **2015**, *21*, 7540−7555. (h) Hernández-Juárez, M.; López-Serrano, J.; González-Herrero, P.; Rendón, N.; Álvarez, E.; Paneque, M.; Suárez, A. Hydrogenation of an Iridium-Coordinated Imidazol-2-ylidene Ligand Fragment. *Chem. Commun.* **2018**, *54*, 3843−3846. (i) Hernández-Juárez, M.; Sánchez, P.; López-Serrano, J.; Lara, P.; González-Herrero, P.; Rendón, N.; Álvarez, E.; Paneque, M.; Suárez, A. Metalated Ir-CNP Complexes Containing Imidazolin-2-ylidene and Imidazolidin-2-ylidene Donors - Synthesis, Structure, Luminescence, and Metal-Ligand Cooperative Reactivity. *Eur. J. Inorg. Chem.* **2020**, *2020*, 3944−3953. (j) Sánchez, P.; Hernández-Juárez, M.; Rendón, N.; López-Serrano, J.; Álvarez, E.; Paneque, M.; Suárez, A. Hydroboration of Carbon Dioxide with Catechol and Pinacol Borane Using an Ir-CNP* Pincer Complex. Water Influence on the Catalytic Activity. *Dalton Trans.* **2018**, *47*, 16766−16776.
(23) Sánchez, P.; Hernández-Juárez, M.; Álvarez, E.; Paneque, M.; Rendón, N.; Suárez, A. Synthesis, Structure and Reactivity of Pd and Ir Complexes Based on New Lutidine-Derived NHC/Phosphine Mixed Pincer Ligands. *Dalton Trans.* **2016**, *45*, 16997−17009.
(24) Sánchez, P.; Hernández-Juárez, M.; Rendón, N.; López-Serrano, J.; Álvarez, E.; Paneque, M.; Suárez, A. Selective, Base-Free Hydrogenation of Aldehydes Catalyzed by Ir Complexes Based on Proton-Responsive Lutidine-Derived CNP Ligands. *Organometallics* **2021**, *40*, 1314−1327.
(25) Sánchez, P.; Hernández-Juárez, M.; Rendón, N.; López-Serrano, J.; Santos, L. L.; Álvarez, E.; Paneque, M.; Suárez, A. Hydrogenation/Dehydrogenation of N-Heterocycles Catalyzed by Ruthenium Complexes Based on Multimodal Proton-Responsive CNN(H) Pincer Ligands. *Dalton Trans.* **2020**, *49*, 9583−9587.
(26) For relevant examples, see: (a) Fogler, E.; Garg, J. A.; Hu, P.; Leitus, G.; Shimon, L. J. W.; Milstein, D. System with Potential Dual Modes of Metal-Ligand Cooperation: Highly Catalytically Active Pyridine-Based PNNH-Ru Pincer Complexes. *Chem. - Eur. J.* **2014**, *20*, 15727−15731. (b) Kar, S.; Rauch, M.; Kumar, A.; Leitus, G.; Ben-David, Y.; Milstein, D. Selective Room-Temperature Hydrogenation of Amides to Amines and Alcohols Catalyzed by a Ruthenium Pincer Complex and Mechanistic Insight. *ACS Catal.* **2020**, *10*, 5511−5515. (c) Srimani, D.; Mukherjee, A.; Goldberg, A. F. G.; Leitus, G.; Diskin-Posner, Y.; Shimon, L. J. W.; Ben-David, Y.; Milstein, D. Cobalt-Catalyzed Hydrogenation of Esters to Alcohols: Unexpected Reactivity Trend Indicates Ester Enolate Intermediacy. *Angew. Chem., Int. Ed.* **2015**, *54*, 12357−12360. (d) Daw, P.; Chakraborty, S.; Garg, J. A.; Ben-David, Y.; Milstein, D. Direct Synthesis of Pyrroles by Dehydrogenative Coupling of Diols and Amines Catalyzed by Cobalt Pincer Complexes. *Angew. Chem., Int. Ed.* **2016**, *55*, 14373−14377. (e) Kumar, A.; Janes, T.; Espinosa-Jalapa, N. A.; Milstein, D. Manganese Catalyzed Hydrogenation of Organic Carbonates to Methanol and Alcohols. *Angew. Chem., Int. Ed.* **2018**, *57*, 12076−1043. (f) Kumar, A.; Espinosa-Jalapa, N. A.; Leitus, G.; Diskin-Posner, Y.; Avram, L.; Milstein, D. Direct Synthesis of Amides by Dehydrogenative Coupling of Amines with either Alcohols or Esters: Manganese Pincer Complex as Catalyst. *Angew. Chem., Int. Ed.* **2017**, *56*, 14992−14996. (g) Espinosa-Jalapa, N. A.; Kumar, A.; Leitus, G.; Diskin-Posner, Y.; Milstein, D. Synthesis of Cyclic Imides by Acceptorless Dehydrogenative Coupling of Diols and Amines Catalyzed by a Manganese Pincer Complex. *J. Am. Chem. Soc.* **2017**, *139*, 11722−11725. (h) Tan, X.; Wang, Y.; Liu, Y.; Wang, F.; Shi, L.; Lee, K.-H.; Lin, Z.; Lv, H.; Zhang, X. Highly Efficient Tetradentate Ruthenium Catalyst for Ester Reduction: Especially for Hydrogenation of Fatty Acid Esters. *Org. Lett.* **2015**, *17*, 454−457. (i) Shi, L.; Tan, X.; Long, J.; Xiong, X.; Yang, S.; Xue, P.; Lv, H.; Zhang, X. Direct Catalytic Hydrogenation of Simple Amides: A Highly Efficient Approach from Amides to Amines and Alcohols. *Chem. - Eur. J.* **2017**, *23*, 546−548.
(27) (a) Rowland, R. S.; Taylor, R. Intermolecular Nonbonded Contact Distances in Organic Crystal Structures: Comparison with Distances Expected from van der Waals Radii. *J. Phys. Chem.* **1996**, *100*, 7384−7391. (b) Reedijk, J. Coordination Chemistry Beyond Werner: Interplay Between Hydrogen Bonding and Coordination. *Chem. Soc. Rev.* **2013**, *42*, 1776−1783.
(28) Kim, S.-K.; Han, W.-S.; Kim, T.-J.; Kim, T.-Y.; Nam, S. W.; Mitoraj, M.; Piekoś, Ł.; Michalak, A.; Hwang, S.-J.; Kang, S. O. Palladium Catalysts for Dehydrogenation of Ammonia Borane with Preferential B-H Activation. *J. Am. Chem. Soc.* **2010**, *132*, 9954−9955.
(29) Staubitz, A.; Sloan, M. E.; Robertson, A. P. M.; Friedrich, A.; Schneider, S.; Gates, P. J.; Auf der Günne, J. S.; Manners, I. Catalytic Dehydrocoupling/Dehydrogenation of *N*-Methylamine-Borane and Ammonia-Borane: Synthesis and Characterization of High Molecular Weight Polyaminoboranes. *J. Am. Chem. Soc.* **2010**, *132*, 13332−13345.
(30) (a) Gómez-Gallego, M.; Sierra, M. A. Kinetic Isotope Effects inthe Study of Organometallic Reaction Mechanisms. *Chem. Rev.* **2011**, *111*, 4857−4963. (b) Simmons, E. M.; Hartwig, J. F. On the Interpretation of Deuterium Kinetic Isotope Effects in C−H Bond Functionalizations by Transition-Metal Complexes. *Angew. Chem., Int. Ed.* **2012**, *51*, 3066−3072.
(31) Espinosa-Jalapa, N. A.; Nerush, A.; Shimon, L. J. W.; Leitus, G.; Avram, L.; Ben-David, Y.; Milstein, D. Manganese-Catalyzed Hydrogenation of Esters to Alcohols. *Chem. - Eur. J.* **2017**, *23*, 5934−5938.
(32) Tejel, C.; del Río, M. P.; Ciriano, M. A.; Reijerse, E. J.; Hartl, F.; Zális, S.; Hetterscheid, D. G. H.; Tsichlis i Spithas, N.; de Bruin, B. Ligand-Centred Reactivity of Bis(picolyl)amine Iridium: Sequential Deprotonation, Oxidation and Oxygenation of a "Non-Innocent" Ligand. *Chem. - Eur. J.* **2009**, *15*, 11878−11889.
(33) Morris, K. F.; Johnson, C. S., Jr. Diffusion-Ordered Two-Dimensional Nuclear Magnetic Resonance Spectroscopy. *J. Am. Chem. Soc.* **1992**, *114*, 3139−3141.

https://doi.org/10.1021/acs.inorgchem.1c03056
Inorg. Chem. 2021, 60, 18490−18502

(34) The X-ray volume ($V_{X\text{-ray}}$) was calculated by dividing the crystallographic unit-cell volume by the number of molecular entities contained in the unit cell, assuming that these have a spherical shape, and subtracting the van der Waals volumes of the THF-solvated K^+ ions. See: Zhao, Y. H.; Abraham, M. H.; Zissimos, A. M. Fast Calculation of van der Waals Volume as a Sum of Atomic and Bond Contributions and Its Application to Drug Compounds. *J. Org. Chem.* **2003**, *68*, 7368−7373.

(35) Rueping, M.; Koenigs, R. M.; Borrmann, R.; Zoller, J.; Weirich, T. E.; Mayer, J. Size-Selective, Stabilizer-Free, Hydrogenolytic Synthesis of Iridium Nanoparticles Supported on Carbon Nanotubes. *Chem. Mater.* **2011**, *23*, 2008−2010.

(36) Ramachandran, P. V.; Gagare, P. D. Preparation of Ammonia Borane in High Yield and Purity, Methanolysis, and Regeneration. *Inorg. Chem.* **2007**, *46*, 7810−7817.

(37) Frisch, M. J.; Trucks, G. W.; Schlegel, H. B.; Scuseria, G. E.; Robb, M. A.; Cheeseman, J. R.; Scalmani, G.; Barone, V.; Petersson, G. A.; Nakatsuji, H.; Li, X.; Caricato, M.; Marenich, A. V.; Bloino, J.; Janesko, B. G.; Gomperts, R.; Mennucci, B.; Hratchian, H. P.; Ortiz, J. V.; Izmaylov, A. F.; Sonnenberg, J. L.; Williams-Young, D.; Ding, F.; Lipparini, F.; Egidi, F.; Goings, J.; Peng, B.; Petrone, A.; Henderson, T.; Ranasinghe, D.; Zakrzewski, V. G.; Gao, J.; Rega, N.; Zheng, G.; Liang, W.; Hada, M.; Ehara, M.; Toyota, K.; Fukuda, R.; Hasegawa, J.; Ishida, M.; Nakajima, T.; Honda, Y.; Kitao, O.; Nakai, H.; Vreven, T.; Throssell, K.; Montgomery, J. A., Jr.; Peralta, J. E.; Ogliaro, F.; Bearpark, M. J.; Heyd, J. J.; Brothers, E. N.; Kudin, K. N.; Staroverov, V. N.; Keith, T. A.; Kobayashi, R.; Normand, J.; Raghavachari, K.; Rendell, A. P.; Burant, J. C.; Iyengar, S. S.; Tomasi, J.; Cossi, M.; Millam, J. M.; Klene, M.; Adamo, C.; Cammi, R.; Ochterski, J. W.; Martin, R. L.; Morokuma, K.; Farkas, O.; Foresman, J. B.; Fox, D. J. *Gaussian 16, Rev. B.01*; Gaussian: Wallingford, CT, 2016.

(38) Yu, H. S.; He, X.; Li, S. L.; Truhlar, D. G. MN15: A Kohn−Sham Global-Hybrid Exchange−Correlation Density Functional with Broad Accuracy for Multi-reference and Single-reference Systems and Noncovalent Interactions. *Chem. Sci.* **2016**, *7*, 5032−5051.

(39) (a) Leininger, T.; Nicklass, A.; Stoll, H.; Dolg, M.; Schwerdtfeger, P. The Accuracy of the Pseudopotential Approximation. II. A Comparison of Various Core Sizes for Indium Pseudopotentials in Calculations for Spectroscopic Constants of InH, InF, and InCl. *J. Chem. Phys.* **1996**, *105*, 1052−1059. (b) Kuchle, W.; Dolg, M.; Stoll, H.; Preuss, H. Energy-Adjusted Pseudopotentials for the Actinides. Parameter Sets and Test Calculations for Thorium and Thorium Monoxide. *J. Chem. Phys.* **1994**, *100*, 7535−7542. (c) Häussermann, U.; Dolg, M.; Stoll, H.; Preuss, H.; Schwerdtfeger, P.; Pitzer, R. M. Accuracy of Energy-Adjusted Quasirelativistic *ab initio* Pseudopotentials. *Mol. Phys.* **1993**, *78*, 1211−1224. (d) Andrae, D.; Häußermann, U.; Dolg, M.; Stoll, H.; Preuß, H. Energy-Adjusted *ab initio* Pseudopotentials for the Second and Third Row Transition Elements. *Theoret. Chim. Acta* **1990**, *77*, 123−141.

(40) Ehlers, A. W.; Böhme, M.; Dapprich, S.; Gobbi, A.; Höllwarth, A.; Jonas, V.; Köhler, K. F.; Stegmann, R.; Veldkamp, A.; Frenking, G. A Set of f-Polarization Functions for Pseudopotential Basis Sets of the Transition Metals Sc-Cu, Y-Ag and La-Au. *Chem. Phys. Lett.* **1993**, *208*, 111−114.

(41) (a) Clark, T.; Chandrasekhar, J.; Spitznagel, G. W.; Schleyer, P. V. R. Efficient Diffuse Function-Augmented Basis Sets for Anion Calculations. III. The 3-21+G Basis Set for First-row Elements, Li−F. *J. Comput. Chem.* **1983**, *4*, 294−301. (b) Francl, M. M.; Pietro, W. J.; Hehre, W. J.; Binkley, J. S.; DeFrees, D. J.; Pople, J. A.; Gordon, M. S. Self-consistent Molecular Orbital Methods. XXIII. A Polarization-type Basis Set for Second-row Elements. *J. Chem. Phys.* **1982**, *77*, 3654−3665. (c) Hariharan, P. C.; Pople, J. A. The Influence of Polarization Functions on Molecular Orbital Hydrogenation Energies. *Theoret. Chim. Acta* **1973**, *28*, 213−222. (d) Hehre, W. J.; Ditchfield, R.; Pople, J. A. Self-Consistent Molecular Orbital Methods. XII. Further Extensions of Gaussian-Type Basis Sets for Use in Molecular Orbital Studies of Organic Molecules. *J. Chem. Phys.* **1972**, *56*, 2257−2261.

(42) Marenich, A. V.; Cramer, C. J.; Truhlar, D. G. Universal Solvation Model Based on Solute Electron Density and on a Continuum Model of the Solvent Defined by the Bulk Dielectric Constant and Atomic Surface Tensions. *J. Phys. Chem. B* **2009**, *113*, 6378−6396.

(43) (a) Fukui, K. The Path of Chemical Reactions - The IRC Approach. *Acc. Chem. Res.* **1981**, *14*, 363−368. (b) Hratchian, H. P., Schlegel, H. B. In *Theory and Applications of Computational Chemistry*; Frenking, G., Kim, K. S., Scuseria, G. E., Eds.; Elsevier: Amsterdam, 2005.

https://doi.org/10.1021/acs.inorgchem.1c03056
Inorg. Chem. 2021, 60, 18490−18502